Cell Reports
Article

Structural Basis for a Reciprocal Regulation between SCF and CSN

Radoslav I. Enchev,[1,2] Daniel C. Scott,[3,4] Paula C.A. da Fonseca,[2] Anne Schreiber,[2,5] Julie K. Monda,[3] Brenda A. Schulman,[3,4,*] Matthias Peter,[1,*] and Edward P. Morris[2,*]
[1]ETH-Zurich, Institute of Biochemistry, Department of Biology, Schafmattstr. 18, CH-8093 Zurich, Switzerland
[2]Division of Structural Biology, The Institute of Cancer Research, Chester Beatty Laboratories, 237 Fulham Road, London SW3 6JB, UK
[3]Department of Structural Biology
[4]Howard Hughes Medical Institute
St. Jude Children's Research Hospital, Memphis, TN 38105, USA
[5]Present address: ETH-Zurich, Institute of Biochemistry, Department of Biology, Schafmattstr. 18, CH-8093 Zurich, Switzerland
*Correspondence: brenda.schulman@stjude.org (B.A.S.), matthias.peter@bc.biol.ethz.ch (M.P.), edward.morris@icr.ac.uk (E.P.M.)
http://dx.doi.org/10.1016/j.celrep.2012.08.019

SUMMARY

Skp1-Cul1-Fbox (SCF) E3 ligases are activated by ligation to the ubiquitin-like protein Nedd8, which is reversed by the deneddylating Cop9 signalosome (CSN). However, CSN also promotes SCF substrate turnover through unknown mechanisms. Through biochemical and electron microscopy analyses, we determined molecular models of CSN complexes with $SCF^{Skp2/Cks1}$ and SCF^{Fbw7} and found that CSN occludes both SCF functional sites—the catalytic Rbx1-Cul1 C-terminal domain and the substrate receptor. Indeed, CSN binding prevents SCF interactions with E2 enzymes and a ubiquitination substrate, and it inhibits SCF-catalyzed ubiquitin chain formation independent of deneddylation. Importantly, CSN prevents neddylation of the bound cullin, unless binding of a ubiquitination substrate triggers SCF dissociation and neddylation. Taken together, the results provide a model for how reciprocal regulation sensitizes CSN to the SCF assembly state and inhibits a catalytically competent SCF until a ubiquitination substrate drives its own degradation by displacing CSN, thereby promoting cullin neddylation and substrate ubiquitination.

INTRODUCTION

Cullin-RING ligases (CRLs) constitute the largest family of E3 ubiquitin ligases (Deshaies and Joazeiro, 2009). The modular CRL architecture explains their pervasive but highly specific functions. As exemplified by the archetypical Skp1-Cullin1-F-box (SCF) complexes, CRLs are nucleated by one of seven structurally elongated cullin protein scaffolds. The conserved cullin C-terminal domain assembles the CRL catalytic core by binding a RING-finger protein, typically Rbx1, which in turn promotes ubiquitin transfer from an associated E2 enzyme. The distal N-terminal end of the cullin binds a substrate receptor (SR) module, which recruits the ubiquitination target. The modular and variable SRs allow recognition of numerous substrates by the same CRL catalytic core.

Human SCF complexes use one of more than 60 SRs, which bind Skp1 through their F-box domain. Skp1 bridges the interaction of Cul1 and the SR, which in turn recruits specific ubiquitination substrates via a distinctive degron motif (Duda et al., 2011). As examples, Fbw7's WD-40 domain recognizes the phosphorylated form of the cell-cycle regulator CyclinE (Hao et al., 2007), while Skp2 uses a leucine-rich repeat domain together with the coreceptor Cks1 to recruit a phosphorylated form of the cyclin-dependent kinase (Cdk) inhibitor p27 (Hao et al., 2005).

CRL catalytic activity is also controlled by covalent attachment of the ubiquitin-like protein Nedd8 to the cullin's winged-helix B (WHB) domain. Similar to ubiquitination, neddylation is mediated by an enzymatic cascade, including the Nedd8-conjugating E2 enzyme Ubc12, which is activated by the RING domain of Rbx1 with stimulation by Dcn1 (Kurz et al., 2005; Scott et al., 2011). Non-neddylated cullin-Rbx1 complexes can bind an inhibitor, CAND1, which prevents neddylation and competes with SR association (Goldenberg et al., 2004). Neddylation favors a conformational rearrangement of the cullin C-terminal domain and Rbx1, which prevents CAND1 binding and enhances CRL-mediated ubiquitination activity (Duda et al., 2008; Saha and Deshaies, 2008; Yamoah et al., 2008).

Cullins are deneddylated by the Cop9 signalosome (CSN). The CSN comprises eight different subunits, Csn1 through Csn8, named in order of descending molecular weight. Together, they unleash the zinc-metalloprotease activity of Csn5 by an unknown mechanism (Sharon et al., 2009). The active site of Csn5 is located within its N-terminal MPN domain (Cope et al., 2002; Lyapina et al., 2001) and most probably functions similarly to the thermolysin-like mechanism described for the homologous deubiquitinating enzyme AMSH-LP (Sato et al., 2008). Csn6 also comprises an MPN domain, which, however, lacks the conserved zinc-coordinating residues and is thus thought to serve a scaffolding function. The remaining six subunits are characterized by PCI domains, comprising a C-terminal winged helix preceded by a bundle of bihelical repeats (Dessau et al., 2008; Scheel and Hofmann, 2005). The PCI domains of Csn1,

Csn2, Csn3, and Csn4 are preceded by long N-terminal extensions, predicted to contain further helical repeats (Enchev et al., 2010; Pick et al., 2009). There is a striking similarity between the CSN subunit composition and that of the lid subcomplex of the 26S proteasome, which also comprises two MPN- and six PCI-domain-containing subunits with 1:1 sequence correspondence (Enchev et al., 2010; Pick et al., 2009).

CAND1 has been implicated in exchange of SRs upon CSN-mediated SCF deneddylation (Schmidt et al., 2009). Thus, SCF regulation has been thought of as a cycle of assembly with SRs, neddylation, substrate ubiquitination, CSN-mediated deneddylation, and CAND1-stimulated disassembly/reassembly and/or neddylation (Bosu and Kipreos, 2008; Cope and Deshaies, 2003). However, in cells, only a small subset of non-neddylated cullins is found in complex with CAND1 (Bennett et al., 2010), and it remains unclear how the neddylation/deneddylation cycle is coordinated with substrate availability. Moreover, cellular CRLs exist in a wide range of assembly states, and upon inhibition of deneddylation, both neddylated and non-neddylated CRLs stably associate with CSN, with or without SR modules (Bennett et al., 2010; Olma et al., 2009). How the different CRL assembly and activation states influence CSN and vice-versa remains poorly understood. Specific signals and SR binding have been suggested as regulators of CSN-CRL4 complex formation (Fischer et al., 2011; Groisman et al., 2003), but neither the structural basis nor the functional significance of forming stable complexes between CSN and the products of its enzymatic reaction is understood. Intriguingly, CRL4 enzymes, which may not require neddylation for activity, can be inhibited through CSN by an unknown mechanism (Fischer et al., 2011). Similarly, a recent study reported that CSN can inhibit SCF activity through a yet unknown, noncatalytic mechanism and that the SCF assembly state influences the CSN deneddylation activity (Emberley et al., 2012). Collectively, the available data imply that CSN and CAND1 regulate CRL function on multiple levels, the relationships and mechanisms of which remain incompletely characterized.

To understand the functional implications of the CSN interactions with CRLs, we determined structures of several CSN and CSN-SCF complexes through electron microscopy. We applied a hybrid structural approach to obtain pseudoatomic molecular models, which were further validated biochemically. Surprisingly, we found that CSN can occlude both SCF functional sites—for E2 enzymes and for ubiquitination substrates—which are located at opposite ends of the SCF complex. Consequently, CSN-SCF complex formation results in inhibited activation of Ubc12 by non-neddylated SCF and of Cdc34 by neddylated SCF and competes with binding to CAND1 and ubiquitination substrate. Our findings thus define the structural and biochemical basis underlying noncatalytic regulation of SCFs by CSN and imply that ubiquitination substrates can trigger SCF activation.

RESULTS

Structural Electron Microscopy Analysis of CSN Complexes

To gain structural and functional insights into the binding of CSN to fully assembled SCFs, we reconstituted various CSN-SCF complexes in vitro. In addition to wild-type CSN, we also produced a recombinant CSN complex harboring a Csn5 subunit with an H138A point mutation in its active site, which interferes with zinc chelation, is deneddylation defective (Cope et al., 2002), and thus stably associates with neddylated SCFs.

Purified complexes of $CSN^{Csn5H138A}$ with neddylated $SCF^{Skp2/Cks1}$ (referred to as $CSN^{Csn5H138A}$-SCF∼$N8^{Skp2/Cks1}$) or SCF^{Fbw7} (referred to as $CSN^{Csn5H138A}$-SCF∼$N8^{Fbw7}$) (Figure 1A) were subjected to negative-stain electron microscopy and single-particle analysis. We determined the structure of the $CSN^{Csn5H138A}$-SCF∼$N8^{Skp2/Cks1}$ complex by ab initio angular reconstitution and iterative rounds of refinement (Figures 1B and S1A). To differentiate between the CSN and SCF components within the map we analyzed electron microscopy images of negatively stained apo CSN complexes. We calculated the structure of apo CSN, using an initial reference derived from the $CSN^{Csn5H138A}$-SCF∼$N8^{Skp2/Cks1}$ structure (Figures 1C and S1B). Comparison between the two maps showed that the apo CSN structure well matched a large portion of the $CSN^{Csn5H138A}$-SCF∼$N8^{Skp2/Cks1}$ map, allowing the segmentation of the latter into its CSN and SCF components (Figure 1D), which was confirmed by difference analysis (Figure S3A). The CSN density is characterized by a well-resolved mesh of discrete patches of elongated densities, consistent with our previous data (Enchev et al., 2010). The remaining region, which therefore corresponds to SCF∼$N8^{Skp2/Cks1}$, forms a separate elongated curved density, connected to CSN through both of its ends.

Next, we investigated whether this CSN-binding mode is structurally conserved among the SCF family through analysis of $CSN^{Csn5H138A}$-SCF∼$N8^{Fbw7}$. The $CSN^{Csn5H138A}$-SCF∼$N8^{Skp2/Cks1}$ structure was used as an initial reference for the analysis of $CSN^{Csn5H138A}$-SCF∼$N8^{Fbw7}$ (Figure S1C). Indeed, the resulting structure (Figure 1E) is overall very similar to $CSN^{Csn5H138A}$-SCF∼$N8^{Skp2/Cks1}$. Difference analysis with the apo CSN map indicated that SCF∼$N8^{Fbw7}$ also employs both of its ends to bind CSN and adopts a comparable position (Figure 1F and Figure S3A).

Molecular Models for CSN and CSN-SCF Complexes

Given the similarity of CSN and the 26S proteasome lid subcomplex (Pick et al., 2009), we considered recent electron microscopy studies defining molecular boundaries of the proteasome lid and proposing pseudoatomic models with constituent subunits for the fission and budding yeast, as well as for human lid subcomplexes (da Fonseca et al., 2012; Lander et al., 2012; Lasker et al., 2012). A comparison of the CSN region of the $CSN^{Csn5H138A}$-SCF∼$N8^{Skp2/Cks1}$ map and the human lid (Figure S2A) revealed substantial similarity. We thus assigned individual subunits within the CSN density to locations corresponding to their homologs in the lid. Atomic models for all human CSN subunits from I-TASSER (Roy et al., 2010) (Figure S2B) were docked into the CSN density. The resulting model (Figure 2) is characterized by a close match between the protein density and the atomic coordinates. There is little density unoccupied by the docked models, and there is no significant spatial overlap between the docked coordinates. Furthermore, the atomic models and the corresponding density segments of the

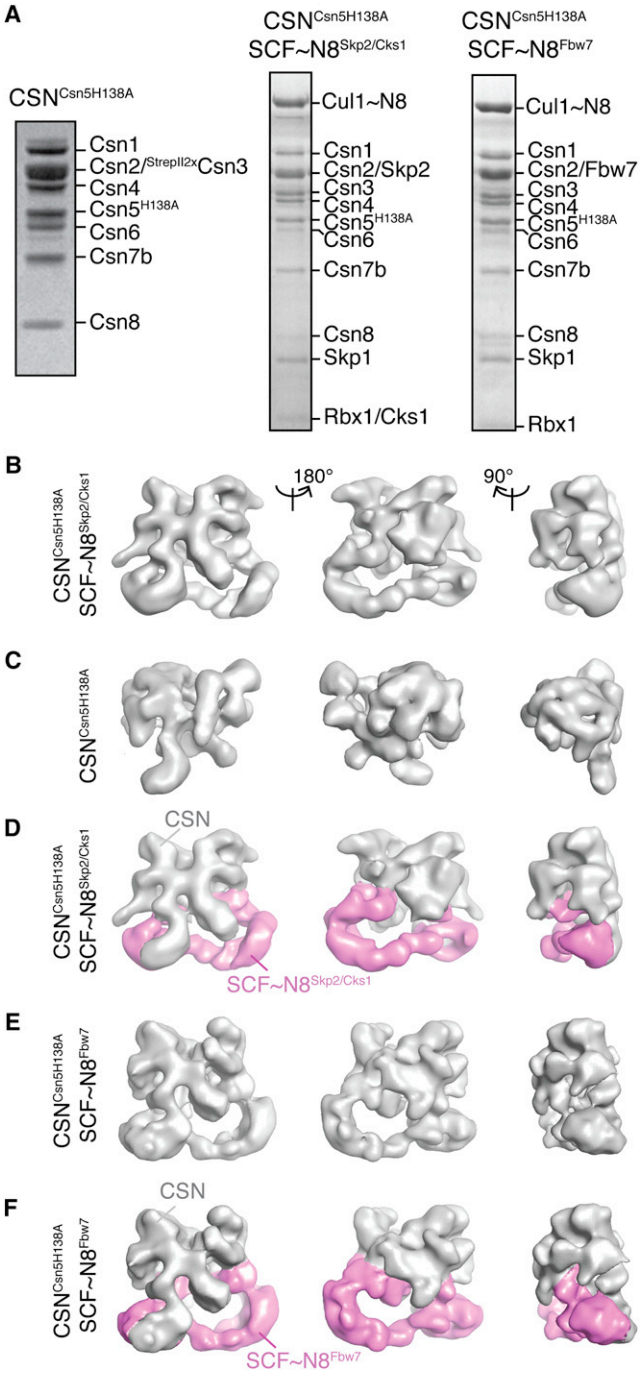

Figure 1. Reconstitution and Single-Particle Electron Microscopy Analysis of CSN-SCF Complexes

(A) Coomassie-stained SDS-PAGE of recombinant CSN^{Csn5H138A} and reconstituted CSN-SCF complexes after gel filtration.

(B–F) Surface views of electron microscopy density maps of (B) CSN^{Csn5H138A}-SCF∼N8$^{Skp2/Cks1}$, (C) CSN^{Csn5H138A}, (D) CSN^{Csn5H138A}-SCF∼N8$^{Skp2/Cks1}$ segmented into its SCF∼N8$^{Skp2/Cks1}$ (purple) and CSN (gray) subcomplexes. (E) CSN^{Csn5H138A}-SCF∼N8^{Fbw7}, and (F) CSN^{Csn5H138A}-SCF∼N8^{Fbw7} segmented into its CSN^{Csn5H138A}-SCF∼N8^{Fbw7} (purple) and CSN (gray) subcomplexes.

See also Figures S1 and S3.

CSN^{Csn5H138A}-SCF∼N8$^{Skp2/Cks1}$ map demonstrate strong correlation (Figure S2D).

In the model, the PCI subunits in CSN form an approximately coplanar surface (Figure 2, right-hand panel). Their major interaction interfaces are formed from the C-terminal winged-helix domains that form an arc (Figure 2, left-hand panel), from which the extended N-terminal domains radiate to form the characteristic ribbon-like densities in the map. In the model, the four longest subunits (Csn1, Csn2, Csn3, and Csn4) are docked into the central region of the arc, which is capped at each end by the shorter Csn7 and Csn8 subunits. The N-terminal peripheral density assigned to Csn4 in the model is less well recovered, possibly due to conformational heterogeneity in this region.

In contrast to the PCI subunits, the MPN subunits Csn5 and Csn6 are predicted to adopt globular conformations (Figure S2B). In the model, these two subunits form a protrusion on the side opposite the PCI subunits (Figure 2, center and right-hand panels), with Csn6 located over the center of the winged-helix arc and Csn5 offset in the direction of the Csn1 and Csn2 N-terminal domains and extending away from the plane of the PCI subunit cluster.

To test the assignments for Csn2 and Csn5, we produced CSN subcomplexes lacking the Csn5 subunit, CSN$^{\Delta Csn5}$, or solely containing the PCI domain of Csn2, CSN$^{Csn2\Delta N1\text{-}269}$ (Figures S1D, S2C, S4F, and S4G). CSN$^{\Delta Csn5}$ formed a complex with SCF∼N8$^{Skp2/Cks1}$ (Figures S3D and 4C). We subjected these complexes to electron microscopy and single-particle analysis. We analyzed CSN$^{\Delta Csn5}$-SCF∼N8$^{Skp2/Cks1}$, using the CSN^{Csn5H138A}-SCF∼N8$^{Skp2/Cks1}$ structure as an initial reference (Figures S1E, S3B, and S3C). The major difference between the refined CSN$^{\Delta Csn5}$-SCF∼N8$^{Skp2/Cks1}$ and CSN^{Csn5H138A}-SCF∼N8$^{Skp2/Cks1}$ maps is that the former lacks density in the region assigned to Csn5 (Figure S3B), which matches well with the Csn5 atomic model. Similarly, we analyzed CSN$^{Csn2\Delta N1\text{-}269}$, using the apo CSN model as a reference (Figure S1F). The resulting map closely resembles the apo CSN structure but lacks a peripheral, extended, and curled density (Figure S3B), which matches well with the location and dimensions of the segment in which we docked the predicted TPR-like fold of the PCI-associated module of Csn2.

Having identified the CSN region in our maps of the CSN-SCF complexes and modeled individual CSN subunits, we interpreted the remaining density in terms of the known atomic structures of SCF components. We generated models for the neddylated SCF complexes on the basis of the SCF$^{Skp2(F\text{-}box\ domain)}$ structure (Zheng et al., 2002) but used a model for the neddylated conformation of the C-terminal domain of Cul1$^{1\text{–}690}$ (Duda et al., 2008) and the structures of the two respective SR assemblies, Skp1-Skp2/Cks1 (Hao et al., 2005; Schulman et al., 2000) and Skp1-Fbw7 (Hao et al., 2007). We docked these as rigid bodies into the corresponding densities of the CSN^{Csn5H138A}-SCF∼N8$^{Skp2/Cks1}$ and CSN^{Csn5H138A}-SCF∼N8^{Fbw7} maps (Figure 3), with close agreement in both cases. The extreme C-terminal domain of Cul1 (Cul1$^{691\text{–}776}$), encompassing Helix29 and WHB, forms one structural entity of a size similar to Rbx1 and Nedd8, and all three are known to be flexibly oriented to each other (Calabrese et al., 2011; Duda et al., 2008; Duda et al., 2012; Fischer et al., 2011), thus precluding their

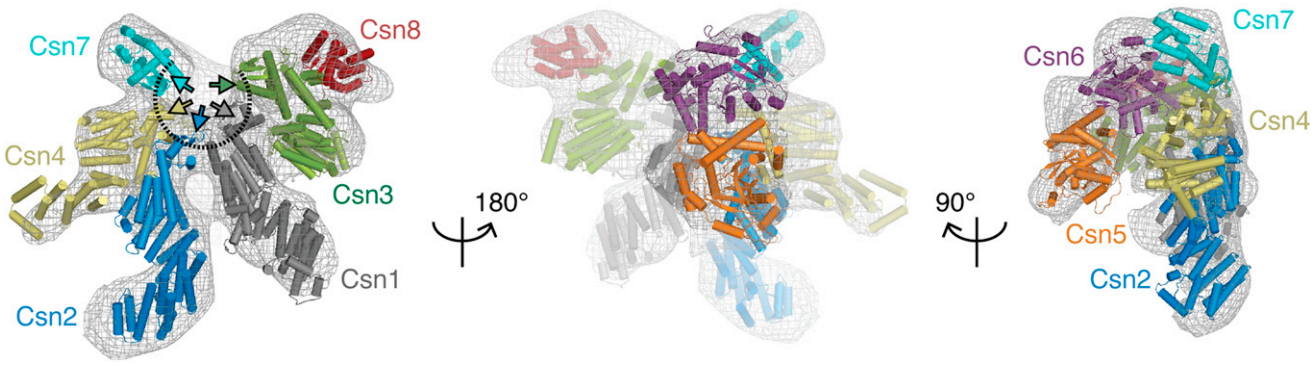

Figure 2. Molecular Model for CSN

The CSN segment from the CSN^{Csn5H138A}-SCF∼N8$^{Skp2/Cks1}$ map is shown as gray mesh. Left, PCI cluster side view. A dotted arc and color-coded arrows indicate the approximately coplanar positions of the winged-helix domains. MPN subunits are omitted for clarity. Center, opposite side, characterized by a protrusion formed by the two MPN domain subunits, Csn5 and Csn6. Right, view showing the edge of the coplanar PCI cluster. The protrusion formed by the Csn5 and Csn6 MPN subunits is left of the PCI cluster. Csn6 is more closely integrated with the PCI cluster, while Csn5 is angled away.
See also Figure S2.

definitive docking in the map. Nevertheless, after the CSN and Cul1$^{1–691}$/Skp1/Skp2/Cks1 segments are assigned, there is a portion of density left unaccounted for (Figure S3D), which matches well a neddylated WHB domain of Cul1 as well as Rbx1. Thus, a putative model is shown in Figures S3E and S3F, demonstrating that WHB∼Nedd8 and Rbx1 can, in principle, be accommodated in the groove between Csn5 and Csn2 (see also Figure 6A).

Both SCF complexes adopt a peripheral position, approaching CSN through their substrate-recognition and E2-binding ends. At the E2-binding end, the Cul1 C-terminal domain and the region of the map modeled as the N-terminal TPR-like domain of Csn2 are connected by a continuous density, which appears to provide the major interaction between SCF and CSN in both complexes (Figure 3). At the substrate-recognition end of the CSN^{Csn5H138A}-SCF∼N8$^{Skp2/Cks1}$ complex, the C-terminal α helices of Skp2 are located between the regions of the map modeled as the N-terminal domains of Csn3 and Csn1 (Figure 3A, middle panel, brown and purple arrows). Analogously, the WD40 repeat domain of Fbw7 is located in the corresponding region in the CSN^{Csn5H138A}-SCF∼N8^{Fbw7} map (Figure 3B, purple arrows). On the other hand, for both CSN^{Csn5H138A}-SCF∼N8$^{Skp2/Cks1}$ and CSN^{Csn5H138A}-SCF∼N8^{Fbw7} complexes, the region into which the Cul1 N-terminal domain and the Skp1 subunit are docked is widely separated from CSN. Hence, it appears unlikely that there is any significant interaction between CSN and either the Cul1 N-terminal domain or the Skp1 subunit.

Determinants and Implications of CSN-SCF Interactions

To test and further explore the observed CSN-SCF interactions, we mixed various CSN and SCF complexes at 1:1 molar ratios and examined association by coelution over analytical size-exclusion chromatography (Figure 4). For comparison, data from the isolated CSN, SCF complexes, or different mutant complexes are shown in Figures S4A–S4E.

Our structural model predicts that CSN predominantly binds to the C-terminal portion of Cul1. Indeed, the coelution profiles observed between CSN^{Csn5H138A} and a complex containing only the C-terminal domain of Cul1 and Rbx1 (Cul1^{CTD}/Rbx1), with and without neddylation, were comparable to the respective full-length Cul1/Rbx1 variants (Figure 4A). On the other hand, modulating the Cul1 C-terminal domain influenced CSN binding. In the presence of CSN^{Csn5H138A}, Cul1/Rbx1 migrated in two peaks, one corresponding to a complex with CSN and the other corresponding to free Cul1/Rbx1 (Figure 4A), while a greater proportion of the neddylated Cul1/Rbx1 (Cul1∼N8/Rbx1) complex copurified with CSN^{Csn5H138A} (Figure 4A). Similarly, neddylated Cul1^{CTD}/Rbx1 complexes showed increased comigration with CSN^{Csn5H138A} compared to non-neddylated controls. Our structural model implies a potentially tenuous contact between CSN and the neddylated WHB domain of Cul1 (WHB∼Nedd8, Figure S3C), and indeed, an intact WHB domain was required for binding of CSN and Cul1/Rbx1 complexes (Figure 4A). However, the WHB domain in isolation does not bind CSN sufficiently strongly to be detected by gel filtration (Figure S4B).

The structural analysis predicts that the Cul1 C-terminal domain approaches Csn2 to form a major interaction (Figure 3). Indeed, CSN$^{Csn2ΔN1–269}$, lacking the N-terminal 269 residues of Csn2, as well as mutants with lesser truncations, failed to coelute with Cul1∼N8/Rbx1 (data not shown) and displayed decreased deneddylation activity, whereas complexes lacking Csn5 generally behaved similarly to CSN^{Csn5H138A} (Figures 4, S2, and S4). Introduction of the Csn5^{H138A} active-site mutation to CSN$^{Csn2ΔN1–269}$ did not restore binding (Figure 4B).

In addition to the CSN-Cul1 C-terminal domain interface, we observed a more tenuous density connecting CSN and the SCF SRs (Figures 3A and 3B). The isolated SR modules Skp1/Skp2/Cks1 and Skp1/Fbw7 did not coelute with CSN, although the SRs appeared to enhance Cul1/Rbx1 association with CSN, since stoichiometric coelution of CSN and SCF$^{Skp2/Cks1}$ or SCF^{Fbw7} over gel filtration did not require neddylation (Figures 4D and 4E). Moreover, the observed interaction of CSN-SCF$^{Skp2/Cks1}$ was not substantially affected by deletion of either WHB or the Rbx1 RING domain (Figure 4E). However,

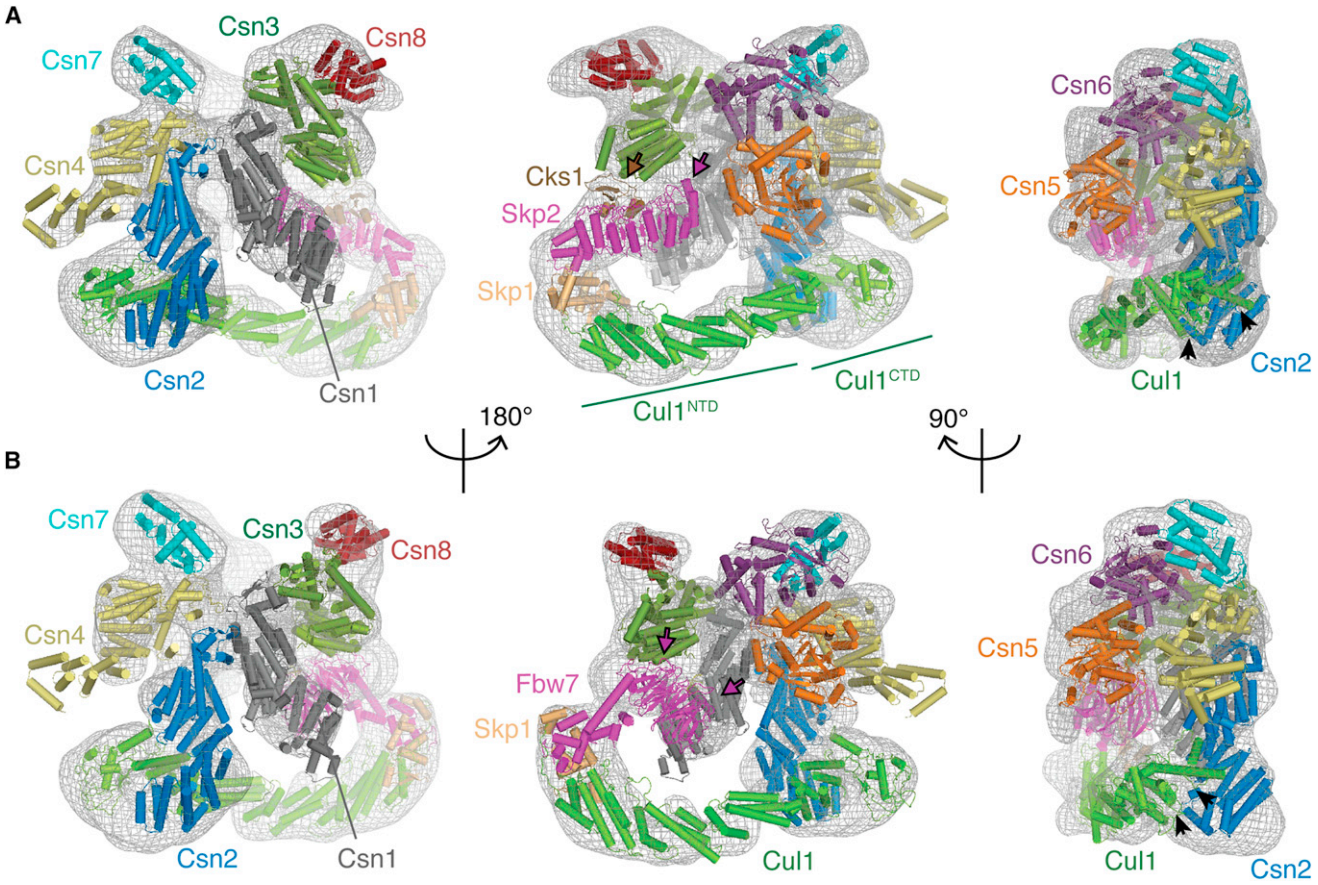

Figure 3. Molecular Models for CSN^{Csn5H138A}-SCF∼N8$^{Skp2/Cks1}$ and CSN^{Csn5H138A}-SCF∼N8^{Fbw7}

(A) Molecular model for CSN^{Csn5H138A}-SCF∼N8$^{Skp2/Cks1}$.

(B) Molecular model for CSN^{Csn5H138A}-SCF∼N8^{Fbw7}.

Brown and purple (A) or purple (B) arrows in the central views indicate contact points between the SCF substrate receptors and CSN. Black arrows in the right-hand views indicate the basic canyon region of Cul1.

See also Figures S1 and S3.

SCF$^{Skp2/Cks1}$ did not coelute with CSN$^{Csn2\Delta N1-104}$ (Figure S4I), confirming that the availability of SR is not sufficient to compensate for the requirement of the Csn2 N-terminal region. The CSN-SCF interaction was further explored by incubating preformed CSN-SCF$^{Skp2/Cks1}$ complexes with CAND1 and analyzing the mix by gel filtration. Interestingly, we observed separation into CSN, CAND1-Cul1/Rbx1, and Skp1/Skp2/Cks1 complexes (Figure S4K).

CSN Can Compete with Ubiquitination Substrate for SCF Binding

Given that CSN approaches SRs in SCF complexes, we examined the potential influence of a ubiquitination substrate. The SCF$^{Skp2/Cks1}$ substrate p27 is phosphorylated prior to SCF binding by Cdks. CyclinA/Cdk2 binds Skp2 and Cks1 and thus forms a complex with SCF$^{Skp2/Cks1}$ and phospho-p27 (p-p27). p27 interacts with both Cdk2 and Skp2/Cks1, but only binding to the latter requires its phosphorylation (Hao et al., 2005; Spruck et al., 2001). The atomic coordinates of CyclinA/Cdk2 (Russo et al., 1996) can be docked onto the SCF$^{Skp2/Cks1}$ structure without steric clashes with other protein densities of our map (Figure 5A). In contrast, modeling the phospho-p27 (p-p27) N- and C-terminal fragments (Hao et al., 2005; Russo et al., 1996) raised the possibility that p-p27 and CSN might bind SCF^{Skp2}-CyclinA/Cdk2/Cks1 in a mutually exclusive manner (Figure 5A, arrow). Likewise, the proximity of CSN to Fbw7 may preclude a full-length substrate protein or protein complex from coexisting with CSN on SCF^{Fbw7} (Figure S6F).

To test whether CSN and p-p27 compete for SCF-binding, we first performed analytical size-exclusion chromatography with equimolar CSN^{Csn5H138A} and SCF^{Skp2}-p-p27/CyclinA/Cdk2/Cks1 in both neddylated and non-neddylated states (Figure 5B). Indeed, CSN^{Csn5H138A} formed a stable complex with SCF∼N8^{Skp2}-CyclinA/Cdk2/Cks1, and p-p27 was excluded from the CSN complexes containing Cul1 (Figures 5B and S5). In the absence of neddylation, SCF^{Skp2}-CyclinA/Cdk2/Cks1 segregated as mutually exclusive complexes with both CSN and p-p27 in a dynamic equilibrium, most likely due to the less stable complex of CSN with non-neddylated SCF^{Skp2}-CyclinA/Cdk2/Cks1 (Figure 5B).

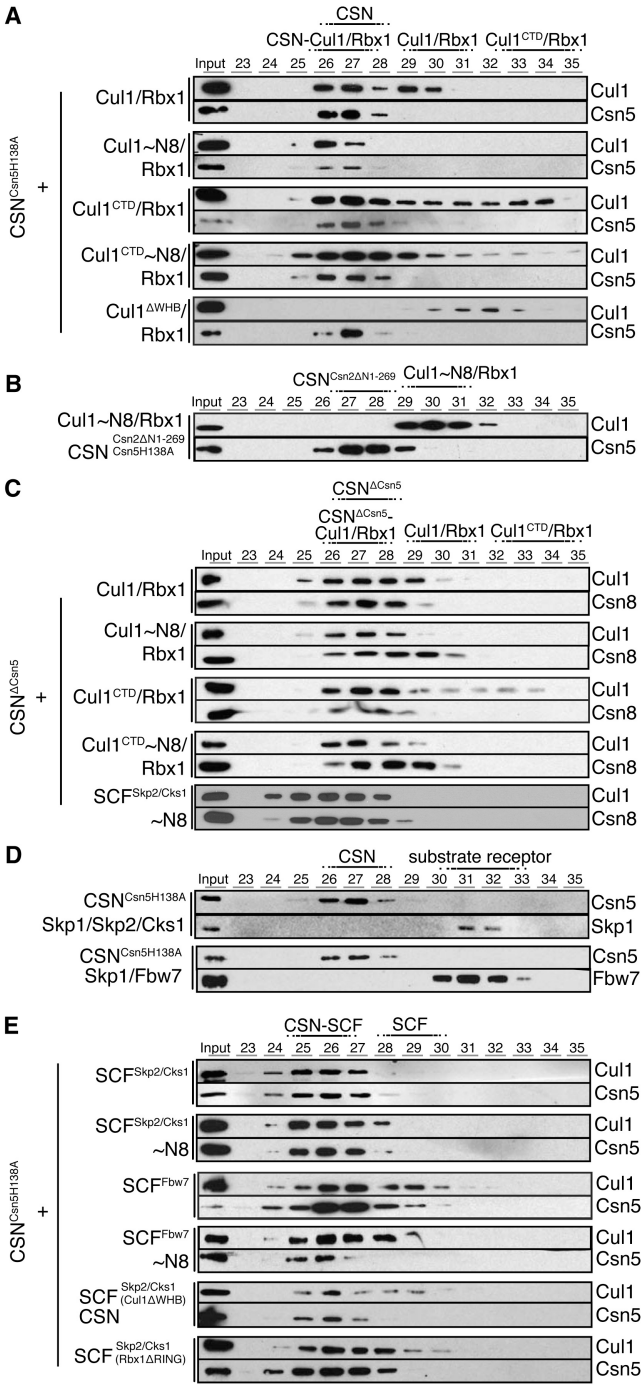

Figure 4. CSN-SCF Interactions Analyzed by Analytical Size-Exclusion Chromatography

Indicated SCF complexes were tested with equimolar amounts of (A, D, E) CSN harboring the Csn5^{H138A} active-site mutation, (B) CSN harboring an N-terminally truncated Csn2 and Csn5^{H138A}, or (C) a CSN complex lacking Csn5. Input and peak fractions (numbered) were blotted with the antibodies indicated to the right. Fractions in which particular complexes were eluted are indicated above each panel. Neddylated complexes are labeled with ~N8.
See also Figure S4.

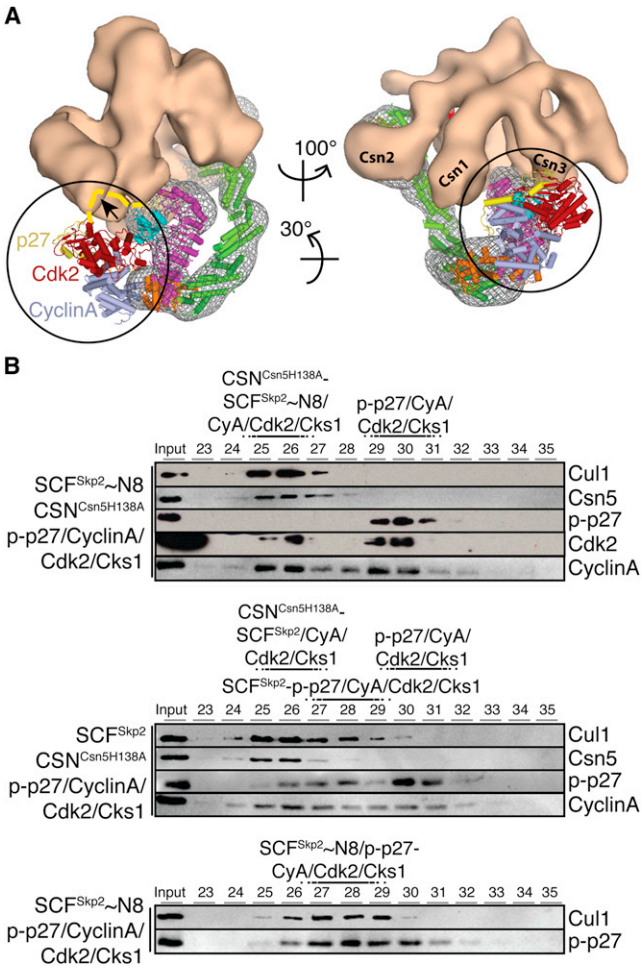

Figure 5. CSN-SCF Interactions in the Presence of Ubiquitination Substrate

(A) Views of the CSN^{Csn5H138A}-SCF~N8$^{Skp2/Cks1}$ map are shown with CSN as an orange surface and SCF$^{Skp2/Cks1}$~N8 as a gray mesh and the atomic coordinates as in Figure 3A. Docked Cdk2 (red), CyclinA (blue), and N- and C-terminal segments of p-p27 (yellow) are indicated by circles. A potential steric clash of p-p27 with the CSN density is indicated by a dashed yellow curve and an arrow on the left.

(B) Neddylated (~N8) or non-neddylated SCF^{Skp2} complexes were incubated with CyclinA/Cdk2/Cks1 and p-p27 in the presence or absence of equimolar amounts of deneddylation-defective CSN^{Csn5H138A} and were analyzed by size-exclusion chromatography.

See also Figure S5.

CSN-Mediated Deneddylation Depends on the SCF Assembly State

To explore the functional effects of different SCF assembly states, we examined CSN deneddylation activity toward different neddylated Cul1/Rbx1 complexes. Because endogenous and recombinant CSN displayed similar deneddylation activities (Figure S6A), all assays were performed with recombinant CSN. Consistent with the finding that the N-terminal domain of Cul1 is not necessary for CSN binding, deneddylation was comparable for neddylated full-length Cul1/Rbx1 (Cul1^{fl}/Rbx1), Cul1^{CTD}/Rbx1, and split-and-coexpressed Cul1/Rbx1 (referred

to here as Cul1^{SCE}/Rbx1) as substrates in our assays (Figure S6A). The latter is obtained by coexpression in bacteria of the Cul1 N-terminal domain (referred to as Cul1^{NTD}), the Cul1 C-terminal domain (referred to as Cul1^{CTD}), and Rbx1 as a total of three separate polypeptides, which assemble into a Cul1^{SCE}/Rbx1 complex whose structural and biochemical properties resemble those of full-length Cul1/Rbx1 (Duda et al., 2008; Goldenberg et al., 2004; Saha and Deshaies, 2008; Zheng et al., 2002).

Interestingly, the deneddylation activity toward Cul1^{SCE}∼N8/Rbx1 was decreased upon addition of stoichiometric amounts of Skp1/Skp2/Cks1 or Skp1/Fbw7 (Figure S6B). Adding CyclinA/Cdk2 strengthened the inhibitory effect of Skp1/Skp2/Cks1, an effect maintained upon further addition of in vitro phosphorylated or unmodified p27 (Figure S6B). These results, which are consistent with a recent biochemical study (Emberley et al., 2012), suggest that Cul1/Rbx1 binding to Skp1/F-box modules, or their complexes with partner proteins, attenuates the deneddylation activity of CSN, possibly through product inhibition. We interpret the lack of deneddylation activity in the presence of substrate as being due to the lack of association between substrate-bound SCFs and CSN (Figure 4B).

CSN-SCF Binding Interferes with Cdc34 Activity

CSN has been shown to impede CRL4 autoubiquitination independently of deneddylation (Fischer et al., 2011). To gain structural insights into whether and how CSN might affect SCF-mediated ubiquitination, we docked the E2 Cdc34 onto the Rbx1 RING domain on the basis of available structures of other E2-RING E3 complexes (Zheng et al., 2000). Although the orientation of Rbx1's RING domain relative to the cullin subunit is known to be flexible (Calabrese et al., 2011; Duda et al., 2008; Fischer et al., 2011), Rbx1 can be positioned as a rigid body together with neddylated Cul1^{CTD} (Duda et al., 2008) with a reasonable fit in the electron microscopy map (Figure S3F). Strikingly, with Rbx1's RING domain in this orientation, or in any other previously reported conformation, steric hindrance would prevent the simultaneous interaction of Cul1/Rbx1 with CSN and Cdc34 (Figure 6A). Moreover, part of the CSN density appears in close proximity to the region most likely corresponding to the basic canyon of Cul1, which recruits the specialized acidic tail of Cdc34 with high affinity (Kleiger et al., 2009) (Figure 3, right-hand panels, black arrows). Structural modeling thus predicts that CSN binding prevents a catalytic interaction of Cul1/Rbx1 and Cdc34. As evident from analytical size exclusion (Figures 5B and S5), CSN and p-p27 binding to neddylated SCF$^{Skp2/Cks1}$ is mutually exclusive. Thus, under the equilibrium conditions of the ubiquitination assays, CSN^{Csn5H138A} or CSN$^{\Delta Csn5}$ is expected to strongly reduce the occupancy time of both p-p27 and Cdc34. Combined with the low efficiency of Cdc34 as a priming E2, addition of these CSN constructs resulted in a decreased length of the polyubiquitin chains assembled by SCF^{Skp2}/Cdc34 on in vitro phosphorylated full-length p27 (p-p27; Figure 6B, left, and Figures S6C and S6D). CSN$^{Csn2\Delta N1-269}$ only partially prevented p-p27 ubiquitination in this lower-molecular-weight region, most likely due to deneddylation by the relatively high and stoichiometric CSN:SCF concentrations used in this assay (Figure S6C).

In cells, CSN's binding to neddylated SCFs would most likely result in very rapid deneddylation (see Figure S6B). To test whether CSN binding can exert an inhibitory effect on non-neddylated SCF, we used an non-neddylatable Cul1 construct with an Arg-to-Lys mutation of its neddylation site (Cul1^{K720R}/Rbx1), which shows residual ubiquitination activity at long time points (Duda et al., 2008; Saha and Deshaies, 2008). This effect was strongly attenuated by stoichiometric addition of CSN^{Csn5H138A} (Figure S6D). The decreased polyubiquitin chain length observed upon addition of CSN^{Csn5H138A} was not due to an obvious contamination with a deubiquitinating enzyme (Figure S6E). Moreover, CSN^{Csn5H138A} counteracts SCF∼N8^{Fbw7} activation of processive Cdc34-mediated ubiquitination of a short Cyclin E phosphopeptide (Figure 6B, right). Notably, because of its small size, this Cyclin E peptide may circumvent the steric clash within the SCF^{Fbw7}-CSN complex, as shown by analytical size-exclusion chromatography (Figures S6F and S6G).

Because the data suggest that CSN interferes with ubiquitin-transfer activity of Cdc34 independent of substrate-SR interactions, we performed pulse-chase assays to monitor SCF-mediated activation of Cdc34's intrinsic ubiquitin-transfer activity. In brief, in the pulse reaction, we generated a thioester-linked Cdc34 conjugate with a ^{32}P-labeled lysine-less (K0) version of ubiquitin. Use of lysine-less ubiquitin prevents polyubiquitin chains from forming during the pulse. In the chase, we added unlabeled wild-type ubiquitin and monitored ligation of radiolabeled K0 ubiquitin by the appearance of diubiquitin chains. Consistent with previous studies, Cdc34-mediated diubiquitin synthesis was stimulated by all complexes containing neddylated Cul1/Rbx1 (Figures 6C and S7A). In addition to neddylated Cul1/Rbx1 itself, this includes neddylated Cul1^{CTD}/Rbx1, SCF$^{Skp2/Cks1}$, and SCF^{Fbw7} (Saha and Deshaies, 2008). Paralleling the effects on substrate ubiquitination, addition of CSN^{Csn5H138A} and CSN$^{\Delta Csn5}$, but not CSN$^{Csn2\Delta N1-269}$, markedly decreased diubiquitin formation (Figure 6C and Figure S7A).

Finally, we used Glmn to probe the accessibility of the RING domain of Rbx1 in the presence or absence of CSN. Glmn can stably interact with the Rbx1 RING domain (Duda et al., 2012), and as with Cdc34, docking its structure onto Rbx1 suggested a steric clash with CSN (Figure S7B). Indeed, addition of Glmn resulted in inhibition of deneddylation, probably due to CSN's inability to bind the Cul1∼N8/Rbx1-Glmn complex. Consistently, an Arg547-to-Ala mutant Glmn impaired for Rbx1 binding did not inhibit CSN deneddylation activity (Figure 6D).

CSN and Ubiquitination Substrate Binding Differentially Regulate SCF Neddylation

The close structural integration of CSN with the Cul1 C-terminal domain-Rbx1 region raises the possibility that CSN binding might also affect neddylation. Indeed, addition of CSN^{Csn5H138A} moderately decreased neddylation of Cul1^{SCE}/Rbx1 and substantially reduced neddylation of Cul1^{SCE}/Rbx1 complexed with Skp1/Skp2/Cks1 (Figure 6E). Addition of Skp1/Skp2/Cks1 as well as CyclinA/Cdk2 in the absence of CSN^{Csn5H138A}, on the other hand, had no major inhibitory effect on Cul1 neddylation (data not shown). Importantly, however, addition of CyclinA/Cdk2 in complex with in vitro phosphorylated p27

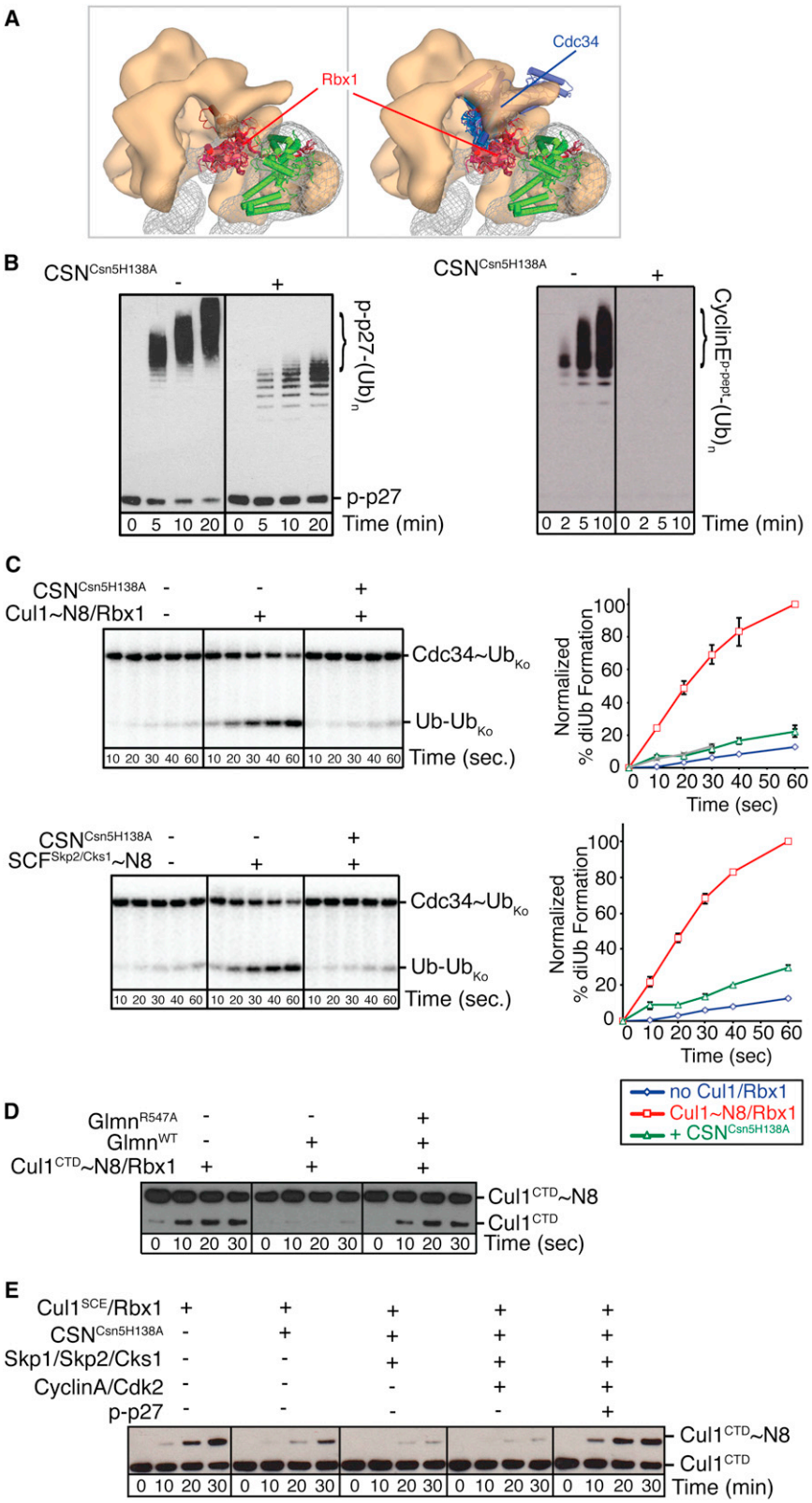

Figure 6. CSN-SCF Binding Regulates Ubiquitination and Neddylation

(A) Zoomed-in surface view of CSN^{Csn5H138A}-SCF~N8$^{Skp2/Cks1}$, color-coded as Figure 5A, showing an overlay of all reported Rbx1 conformations without (left) or with (right) the docked Cdc34 model. Cul1$^{411–690}$ (C-terminal domain without Helix29 and WHB) is shown in green, Rbx1 and Cds34 orientations are shown as hues of red and blue.

(B) In vitro ubiquitination of p-p27 (left) CyclinE^{phosphopeptide} (right), assayed in the absence (–) or presence (+) of catalytically inactive CSN^{Csn5H138A}. Unmodified and polyubiquitinated substrates [–(Ub)$_n$] were detected by immunoblotting with p-p27 antibodies and biotin antibodies, respectively.

(C) Pulse-chase [^{32}P]~ubiquitin (Ub) transfer from Cdc34 to lysine-less ubiquitin (Ub$_{K0}$) in the presence (+) or absence (–) of CSN^{Csn5H138A} and neddylated Cul1/Rbx1 (upper panel) or neddylated SCF$^{Skp2/Cks1}$ (lower panel). Formation of di-Ub was assayed by autoradiography (left-hand panels) and quantified by plotting the percentage of di-Ub formation as a function of time (right-hand panels).

(D) Deneddylation of Cul1^{CTD}~N8/Rbx1 by CSN was assayed as described in Figure S6B in the presence (+) or absence (–) of wild-type (WT) or Rbx1-interaction-defective R547A mutant Glmn.

(E) Neddylation (~N8) of Cul1^{SCE}/Rbx1 was measured by immunoblotting with Cul1 antibodies, in the presence (+) or absence (–) of CSN^{Csn5H138A}, Skp1/Skp2/Cks1, and CyclinA/Cdk2 and p-p27.

See also Figures S6 and S7.

relieves the CSN^{Csn5H138A}-mediated inhibition of neddylation (Figure 6E). These experiments support the notion that CSN inhibits neddylation of bound SCF complexes by blocking access to Ubc12, implying that CSN couples SCF neddylation with substrate availability.

DISCUSSION

Recent studies showing that over 30% of cellular CRLs exist in stable complexes with CSN demonstrate that CRLs and CSN do not interact only as short-lived catalytic intermediates (Olma et al., 2009; Bennett et al., 2010). Here, we report molecular models of CSN in complex with two fully assembled SCFs, which provide a structural framework for understanding stable CSN-SCF species and, combined with biochemical assays, reveal unexpected noncatalytic modes of SCF regulation by CSN.

Molecular Architecture of CSN

The proposed molecular model for CSN provides a glimpse into the overall three-dimensional arrangement of the eight CSN subunits. We have experimentally validated the global locations of Csn2 and Csn5 and docked homology models into the corresponding segments (Figure S2D). Although the docking statistics for the remaining subunits appear to be of similarly high quality, we note that the models are only predictions and that their exact conformation and/or orientation cannot be determined at the resolution of the present study. Nevertheless, our model is supported by the strong similarity between the density distribution of the CSN complex described here and that of its homolog, the lid of the 26S proteasome, whose subunit arrangement has been established at higher resolution (Figure 2A) (da Fonseca et al., 2012; Lander et al., 2012; Lasker et al., 2012). Furthermore, our model is supported by most available subunit-interaction data. For example, the subunit proximities match well with the tandem mass spectrometry analysis of recombinantly produced and reconstituted CSN (Sharon et al., 2009) as well as additional subunit contacts, including Csn1-Csn4 and Csn2-Csn4 (Serino et al., 2003; Tsuge et al., 2001). In our model, interaction between Csn1 and Csn2 involves their C-terminal winged-helix domains in agreement with the experimental observation that their PCI domains are sufficient for incorporation into the complex, whereas their N-terminal portions do not copurify with CSN (Tsuge et al., 2001; Yang et al., 2002). In fact, a splice variant of Csn2, known as Alien, is missing the winged-helix domain and functions as a CSN-independent corepressor of the thyroid hormone receptor (Tenbaum et al., 2003). Indeed, our model is consistent with the major interactions among the elongated PCI-domain-containing subunits Csn1, Csn2, Csn3, and Csn4 being through their winged-helix domains (Figure 2). Interestingly, although the overall molecular architectures of CSN and the proteasome lid are strikingly similar, these two complexes appear to recognize their substrates by different structural elements. While CSN requires the N terminus of Csn2 to position the neddylated cullin C-terminal domain in proximity to Csn5 (Figure 3), the proteasome paralog of Csn2, Rpn6, is a scaffold, linking the lid to the 20S core. Recognition of polyubiquitinated substrates relies on nonlid subunits such as Rpn10 and Rpn13.

Molecular Determinants of the CSN-SCF Interaction

No structural information for a CSN-CRL interaction was previously available. Extrapolating from X-ray crystallographic data for other CRL-binding partners, one might have predicted either a relatively narrow interface, as observed between Cul1/Rbx1 and E2 enzymes and/or Dcn1, or a very broad interface engulfing most of the cullin, as for Cand1 (Duda et al., 2011). However, our structural and biochemical analysis revealed that CSN localizes to both SCF functional sites. In our model, this two-pronged interaction between CSN and SCF involves primarily the Csn2/Csn5 region and the cullin C-terminal domain, as well as the Csn1/Csn3 region and the SCF SR (Figure 3).

Interestingly, our data revealed that Csn5 is dispensable for assembly of the remaining seven subunits, consistent with its peripheral location in the complex (Figure 2) and the fact that such a Csn5-free CSN subcomplex can still bind SCF but not deneddylate it (Figures 4C and S4G). Furthermore, cullin neddylation stabilized the CSN-SCF interaction, even in the absence of Csn5 (Figure 4), suggesting that a Csn5-Nedd8 contact is not essential for the interaction. It seems likely that Csn2, and perhaps other CSN subunits, preferentially binds to the neddylated conformation of the cullin C-terminal domain and/or Rbx1. Notably, although Csn5 harbors a catalytic JAMM motif, the subunit has to be assembled in the CSN complex for deneddylation to be observed (Sharon et al., 2009). Our molecular model thus suggests an unexpected explanation: Csn5 itself cannot recognize neddylated SCF substrates but apparently requires Csn2 and the rest of the complex to position the Nedd8 moiety attached to the CRL correctly in its active site. Moreover, this result implies that in contrast to Csn2, depletion of Csn5 or addition of chemical Csn5 inhibitors may not affect the formation rate or stability of CSN-CRL complexes in cells. Importantly, in our in vitro assays, loss of Csn5 had no effect on the noncatalytic modes of CSN-mediated SCF inhibition. We therefore caution against using Csn5 depletion or chemical inhibition as the sole means of inactivating CSN function.

We also identified CSN-density segments modeled as Csn1 and Csn3 as approaching the SCF SRs, consistent with binding of a beta-barrel SR and Csn1 (Tsuge et al., 2001). Indeed, we observed small structural differences in the densities assigned to the N termini of Csn1 and Csn3 between the apo CSN and the CSN-SCF complexes (Figure S3A), which may indicate conformational rearrangements associated with SCF binding and are reminiscent of the conformational changes reported for binding of the lid to the proteasome (Lander et al., 2012). However, this interaction appears less substantial than the Csn2-dependent Cul1 C-terminal domain interaction (Figure 3), and when examined by analytical size-exclusion chromatography (Figure 4B) and pull-down assays (not shown), CSN does not appreciably associate with SRs in the absence of Cul1/Rbx1. Nevertheless, the presence of SRs increases Cul1/Rbx1 association with CSN (Figure 4). Intriguingly, CSN can preferentially form complexes with CRL subsets, determined partly by the identity of the SRs (Olma et al., 2009). Additional studies are needed in order to shed light on the structural basis for such preferences and their functional implications.

CSN Regulates SCF Activity by Multiple Mechanisms

The functional significance of the prevalent CSN-CRL complexes found in cells has remained poorly understood. The structural models presented here suggest a surprisingly complex, multilayered mechanism of CSN-mediated inhibition of SCF activity. Apart from deneddylation, our data suggest that CSN binding exerts a double-pronged attack on both SCF functional sites by sterically hindering productive interactions of SCF with other factors. Indeed, we demonstrate that CSN competes with the Rbx1 RING interactors Glmn (Duda et al., 2012; Tron et al., 2012), the ubiquitin E2 enzyme Cdc34, and the Nedd8-E2 Ubc12, as well as a ubiquitination substrate. Other RING interactors have also been shown to interfere with CSN-mediated deneddylation (Emberley et al., 2012). Consistently, we showed that CSN binding is sufficient to inhibit SCF-mediated ubiquitination, even when catalytically inactive $CSN^{Csn5H138A}$ complexes are used. Importantly, wild-type CSN has been reported to inhibit CRL4 ubiquitination activity by an unknown, noncatalytic mechanism (Fischer et al., 2011), suggesting that CSN inhibition mediated by steric hindrance is conserved across the CRL family.

CSN and CAND1 Differentially Regulate CRL Assembly and Activity

Very little is known about the regulation of CSN activity. Unexpectedly, we observe that the assembly of Cul1/Rbx1 with SRs also downregulates the deneddylation activity of CSN, implying that SR-free cullins are better deneddylation substrates. This is consistent with findings that binding to SRs correlates with increased Cul1/Rbx1 neddylation in cells (Chew and Hagen, 2007; Kawakami et al., 2001). Together, our data provide the structural and mechanistic basis for a two-branched model of regulating SCF assembly and ubiquitination activity by CSN and CAND1, which may have evolved to regulate distinct Cul1/Rbx1 assemblies. CAND1 recognizes non-neddylated Cul1/Rbx1 complexes, and its interaction with Cul1/Rbx1 is in a dynamic equilibrium with the Cul1/Rbx1-Skp1/F-box interaction, thereby facilitating reassembly of non-neddylated cullins with SR modules (Bornstein et al., 2006; Schmidt et al., 2009; Siergiejuk et al., 2009) (Figure S4K; D.C.S. and B.A.S., unpublished data). We presume that there are no protein factors favoring directionality in the equilibrium. On the other hand, CSN regulates the ubiquitination activity of assembled SCFs through the multiple mechanisms detailed above. Importantly, in addition to deneddylation, the CSN-SCF interaction inhibits Rbx1-Ubc12-mediated Cul1 neddylation, thereby sequestering and protecting assembled SCF complexes in an inactive state.

CRL Activation Requires Dissociation of CSN-CRL Complexes

Our work implies that the prevalent stably bound SCF-CSN complexes in cells (Bennett et al., 2010) are in a reciprocally inactivated state, which raises the question of how SCF-CSN complexes dissociate. The formation of CSN-CRL4s plays regulatory roles in the cellular response to DNA damage (Groisman et al., 2003)—a complex cellular process, meticulously regulated by post-translational modifications. It is thus conceivable that, for example, phosphorylation of the CSN-CRL-binding interface could influence complex formation. Indeed, several kinases associate with CSN and have been shown to phosphorylate Csn2 and Csn7 (Sun et al., 2002; Uhle et al., 2003; Wilson et al., 2001). Moreover, Csn1, Csn3, and Csn8 have also been shown to be phosphorylation targets (Fang et al., 2008; Matsuoka et al., 2007). It will thus be important to investigate whether post-translational modifications could disrupt interaction interfaces between CSN and CRLs and thus play broad roles in negatively regulating their association.

Interestingly, our data suggest that CSN and the ubiquitination substrate p27 compete for $SCF^{Skp2/Cks1}$-binding (Figure 5). Similarly, addition of the SCF^{Fbw7} substrate phospho-CyclinE/Cdk2 downregulates deneddylation (Emberley et al., 2012). Moreover, CRL4 binding to chromatin-located substrates has been proposed to trigger to CSN-CRL4 dissociation (Fischer et al., 2011). Thus, the levels of ubiquitination substrates might also regulate CSN-CRL dissociation in vivo. Consistent with this notion, substrate-bound CRLs are fully neddylated in cells (Read et al., 2000). Here, we show that substrate promotes Cul1 neddylation even in the presence of catalytically inactive CSN. In cells, substrate-favored dissociation of CSN-SCF complexes could both allow neddylation and further promote polyubiquitination and proteasomal degradation of the substrate. CSN binding may prevent a futile neddylation/deneddylation cycle by coupling cullin neddylation to substrate availability. Unidirectionality may be further programmed by CSN's failure to deneddylate substrate-bound SCFs. Our data suggest that the molecular architecture of CSN is better suited to stably bind fully assembled SCFs rather than SR-free cullins. We therefore propose that CSN acts as a sensor for catalytically assembled SCFs and protects these complexes from disassembly, neddylation, and ubiquitin-mediated degradation until critical amounts of the cognate ubiquitination substrate have accumulated. In this model, CSN would not only work as an inhibitor of SCF activity but would also promote SCF function by maintaining its assembly in a state that ensures rapid and efficient substrate turnover.

EXPERIMENTAL PROCEDURES

Cloning, Expression, Purification, and Immunoblotting

Full description is provided in the Extended Experimental Procedures.

Analytical Size-Exclusion Chromatography

Protein concentrations were measured with a NanoDrop (Thermo Scientific) in 6 M guanidine. Equimolar (1 μM) CSN and Cul1/Rbx1 variants were mixed on ice for 10 min in 15 mM HEPES, pH 7.8, 150 mM NaCl, 1% glycerol, 1 mM DTT. Skp1/Skp2/Cks1, p27/CyclinA/Cdk2 and/or CAND1 were added in slight excess (1.2 μM). Nedd8, the WHB domain of Cul1 were added at 5 μM. 200 μl protein mixture was injected onto a Superose 6 10/300 size-exclusion column (GE Healthcare); the run was performed at 4°C, collecting 48 500 μl fractions. Aliquots were analyzed by SDS PAGE on 4%–12% or 12% gels and immunoblotting.

Neddylation and Deneddylation Assays

Cul1/Rbx1 purified from insect cells (Enchev et al., 2010) and all other Cul1/Rbx1 constructs were neddylated by incubating 8 μM $Cul1^{fl}$/Rbx1; 500 nM APPBP1-Uba3; 1 μM Ubc12; 10 μM Nedd8 at room temperature for 10 min in 50 mM Tris/HCl, pH 7.6, 100 mM NaCl, 2.5 mM $MgCl_2$, 150 μM ATP. After addition of 10 mM DTT, products were purified over a Superdex 200 column (Duda et al., 2008). Neddylation assays involving $CSN^{Csn5H138A}$

addition contained 25 nM APPBP1/Uba3, 125 nM Ubc12, 125 nM Cul1/Rbx1, +/− 125 nM Skp1/Skp2/Cks1, +/− 1 μM or 3 μM CyclinA/Cdk2 or CyclinA/Cdk2/p-p27 in 25mM Tris pH 7.0, 50mM NaCl, 10mM $MgCl_2$, 1.5mM ATP, incubated on ice for 20 min. $CSN^{Csn5H138A}$ was then added at 500 nM and incubated on ice for 5 min. Reactions were initiated by addition of 20 μM Nedd8. Aliquots were analyzed by SDS PAGE on 4%–12% gels and immunoblotting.

Deneddylation assays were performed in 50mM Tris, 50mM NaCl pH = 7.6 at room temperature using 2 nM CSN variants and 150 nM neddylated Cul1/Rbx1 variants and Skp1/F-box. 800nM CyclinA/Cdk2, CyclinA/Cdk2/p27, or CyclinA/Cdk2/p-p27 was added to ensure complex formation with Skp1/Skp2.

Ubiquitination Assays

Ubiquitination assays were performed at room temperature with 200 nM SCF variants and 100 nM UbE1, 500 nM Cdc34 and 50 μM ubiquitin. p27 was phosphorylated in vitro for 30 min at 30°C by mixing 4 μM CyclinA/Cdk2 and p27 in 40 mM Tris/HCl, pH 7.6, 10 mM $MgCl_2$, 1 mM ATP and 1 mM DTT. 200 nM phospho-p27/CyclinA/Cdk2 or 5 μM biotinylated CyclinE phosphopeptide were used as substrates. 500 nM (Figure 6B and S6C) or 200 nM (Figure S6D) CSN variants were added as indicated. Aliquots were analyzed by SDS PAGE on 4%–12% gels immunoblotting.

Diubiquitin Formation Assays

10 μM Cdc34 was loaded with 20 μM lysine-less [^{32}P]-ubiquitin ([^{32}P]-Ub^{R7}) with 100 nM ubiquitin E1 in 50 mM HEPES, pH 7.5, 200 mM NaCl, 10 mM $MgCl_2$, 1.5 mM ATP at room temperature for 25 min. The loading reaction was quenched by the addition of EDTA to 50 mM. Discharge reactions were performed in 25 mM Tris pH7.6, 100 mM NaCl, 50 mM EDTA. 250 nM ubiquitin, 500 nM Cul1∼N8/Rbx1 +/− a 1:1 mix of Skp1/F-box were incubated on ice for 30 min to equilibrate SCF complex formation. The mixtures were placed at room temperature, and after a 5 min incubation, the indicated CSN variants were added to a final concentration of 1.25 μM followed by an additional 5 min incubation at room temperature. Discharge was initiated by the addition of Cdc34∼[^{32}P]Ub^{R7} to a final concentration of 400 nM. Aliquots were analyzed on 4%–12% gels, dried, and exposed to a phosphoimager screen, scanned on a StormImager and quantified using ImageQuant TL v2003.02.

Electron Microscopy and Single-Particle Analysis

Electron microscopy data collection and analysis were similar to that described in (Enchev et al., 2010). Detailed description is given in the Extended Experimental Procedures.

ACCESSION NUMBERS

$CSN^{Csn5H138A}$-SCF∼$N8^{Skp2/Cks1}$ has been deposited in the EMDataBank under accession code EMD-2173, $CSN^{Csn5H138A}$-SCF∼$N8^{Fbw7}$ under EMD-2174, $CSN^{\Delta Csn5}$-SCF∼$N8^{Skp2/Cks1}$ under EMD-2175, CSN under EMD-2176, and $CSN^{Csn2\Delta N1-269}$ under EMD-2177.

SUPPLEMENTAL INFORMATION

Supplemental Information includes Extended Experimental Procedures and seven figures and can be found with this article online at http://dx.doi.org/10.1016/j.celrep.2012.08.019.

LICENSING INFORMATION

ACKNOWLEDGMENTS

We thank D. Barford for providing access to equipment and laboratory space, F. Beuron for EM support, and R. Deshaies and A. Smith for critical reading. R.I.E. is funded by an ETH/Marie Curie fellowship. E.P.M. is supported by the ICR; M.P. by the Swiss National Science Foundation, an ERC senior award, and the ETH-Zurich; and B.A.S. by ALSAC, HHMI, and NIH grant R01GM069530. B.A.S. is an Investigator of the Howard Hughes Medical Institute.

Received: August 15, 2012
Revised: August 24, 2012
Accepted: August 24, 2012
Published online: September 6, 2012

REFERENCES

Bennett, E.J., Rush, J., Gygi, S.P., and Harper, J.W. (2010). Dynamics of cullin-RING ubiquitin ligase network revealed by systematic quantitative proteomics. Cell *143*, 951–965.

Bornstein, G., Ganoth, D., and Hershko, A. (2006). Regulation of neddylation and deneddylation of cullin1 in SCFSkp2 ubiquitin ligase by F-box protein and substrate. Proc. Natl. Acad. Sci. USA *103*, 11515–11520.

Bosu, D.R., and Kipreos, E.T. (2008). Cullin-RING ubiquitin ligases: global regulation and activation cycles. Cell Div. *3*, 7.

Calabrese, M.F., Scott, D.C., Duda, D.M., Grace, C.R., Kurinov, I., Kriwacki, R.W., and Schulman, B.A. (2011). A RING E3-substrate complex poised for ubiquitin-like protein transfer: structural insights into cullin-RING ligases. Nat. Struct. Mol. Biol. *18*, 947–949.

Chew, E.H., and Hagen, T. (2007). Substrate-mediated regulation of cullin neddylation. J. Biol. Chem. *282*, 17032–17040.

Cope, G.A., and Deshaies, R.J. (2003). COP9 signalosome: a multifunctional regulator of SCF and other cullin-based ubiquitin ligases. Cell *114*, 663–671.

Cope, G.A., Suh, G.S., Aravind, L., Schwarz, S.E., Zipursky, S.L., Koonin, E.V., and Deshaies, R.J. (2002). Role of predicted metalloprotease motif of Jab1/Csn5 in cleavage of Nedd8 from Cul1. Science *298*, 608–611.

da Fonseca, P.C., He, J., and Morris, E.P. (2012). Molecular model of the human 26S proteasome. Mol. Cell *46*, 54–66.

Deshaies, R.J., and Joazeiro, C.A. (2009). RING domain E3 ubiquitin ligases. Annu. Rev. Biochem. *78*, 399–434.

Dessau, M., Halimi, Y., Erez, T., Chomsky-Hecht, O., Chamovitz, D.A., and Hirsch, J.A. (2008). The Arabidopsis COP9 signalosome subunit 7 is a model PCI domain protein with subdomains involved in COP9 signalosome assembly. Plant Cell *20*, 2815–2834.

Duda, D.M., Borg, L.A., Scott, D.C., Hunt, H.W., Hammel, M., and Schulman, B.A. (2008). Structural insights into NEDD8 activation of cullin-RING ligases: conformational control of conjugation. Cell *134*, 995–1006.

Duda, D.M., Scott, D.C., Calabrese, M.F., Zimmerman, E.S., Zheng, N., and Schulman, B.A. (2011). Structural regulation of cullin-RING ubiquitin ligase complexes. Curr. Opin. Struct. Biol. *21*, 257–264.

Duda, D.M., Olszewski, J.L., Tron, A.E., Hammel, M., Lambert, L.J., Waddell, M.B., Mittag, T., Decaprio, J.A., and Schulman, B.A. (2012). Structure of a Glomulin-RBX1-CUL1 Complex: Inhibition of a RING E3 Ligase through Masking of Its E2-Binding Surface. Mol. Cell *47*, 371–382.

Emberley, E.D., Mosadeghi, R., and Deshaies, R.J. (2012). Deconjugation of Nedd8 from Cul1 is directly regulated by Skp1-Fbox and substrate, and CSN inhibits deneddylated SCF by a non-catalytic mechanism. J Biol. Chem. Published online July 5, 2012. http://dx.doi.org/10.1074/jbc.M112.352484.

Enchev, R.I., Schreiber, A., Beuron, F., and Morris, E.P. (2010). Structural insights into the COP9 signalosome and its common architecture with the 26S proteasome lid and eIF3. Structure *18*, 518–527.

Fang, L., Wang, X., Yamoah, K., Chen, P.L., Pan, Z.Q., and Huang, L. (2008). Characterization of the human COP9 signalosome complex using affinity purification and mass spectrometry. J. Proteome Res. *7*, 4914–4925.

Fischer, E.S., Scrima, A., Böhm, K., Matsumoto, S., Lingaraju, G.M., Faty, M., Yasuda, T., Cavadini, S., Wakasugi, M., Hanaoka, F., et al. (2011). The

molecular basis of CRL4DDB2/CSA ubiquitin ligase architecture, targeting, and activation. Cell *147*, 1024–1039.

Goldenberg, S.J., Cascio, T.C., Shumway, S.D., Garbutt, K.C., Liu, J., Xiong, Y., and Zheng, N. (2004). Structure of the Cand1-Cul1-Roc1 complex reveals regulatory mechanisms for the assembly of the multisubunit cullin-dependent ubiquitin ligases. Cell *119*, 517–528.

Groisman, R., Polanowska, J., Kuraoka, I., Sawada, J., Saijo, M., Drapkin, R., Kisselev, A.F., Tanaka, K., and Nakatani, Y. (2003). The ubiquitin ligase activity in the DDB2 and CSA complexes is differentially regulated by the COP9 signalosome in response to DNA damage. Cell *113*, 357–367.

Hao, B., Zheng, N., Schulman, B.A., Wu, G., Miller, J.J., Pagano, M., and Pavletich, N.P. (2005). Structural basis of the Cks1-dependent recognition of p27(Kip1) by the SCF(Skp2) ubiquitin ligase. Mol. Cell *20*, 9–19.

Hao, B., Oehlmann, S., Sowa, M.E., Harper, J.W., and Pavletich, N.P. (2007). Structure of a Fbw7-Skp1-cyclin E complex: multisite-phosphorylated substrate recognition by SCF ubiquitin ligases. Mol. Cell *26*, 131–143.

Kawakami, T., Chiba, T., Suzuki, T., Iwai, K., Yamanaka, K., Minato, N., Suzuki, H., Shimbara, N., Hidaka, Y., Osaka, F., et al. (2001). NEDD8 recruits E2-ubiquitin to SCF E3 ligase. EMBO J. *20*, 4003–4012.

Kleiger, G., Saha, A., Lewis, S., Kuhlman, B., and Deshaies, R.J. (2009). Rapid E2-E3 assembly and disassembly enable processive ubiquitylation of cullin-RING ubiquitin ligase substrates. Cell *139*, 957–968.

Kurz, T., Ozlü, N., Rudolf, F., O'Rourke, S.M., Luke, B., Hofmann, K., Hyman, A.A., Bowerman, B., and Peter, M. (2005). The conserved protein DCN-1/Dcn1p is required for cullin neddylation in C. elegans and S. cerevisiae. Nature *435*, 1257–1261.

Lander, G.C., Estrin, E., Matyskiela, M.E., Bashore, C., Nogales, E., and Martin, A. (2012). Complete subunit architecture of the proteasome regulatory particle. Nature *482*, 186–191.

Lasker, K., Förster, F., Bohn, S., Walzthoeni, T., Villa, E., Unverdorben, P., Beck, F., Aebersold, R., Sali, A., and Baumeister, W. (2012). Molecular architecture of the 26S proteasome holocomplex determined by an integrative approach. Proc. Natl. Acad. Sci. USA *109*, 1380–1387.

Lyapina, S., Cope, G., Shevchenko, A., Serino, G., Tsuge, T., Zhou, C., Wolf, D.A., Wei, N., Shevchenko, A., and Deshaies, R.J. (2001). Promotion of NEDD-CUL1 conjugate cleavage by COP9 signalosome. Science *292*, 1382–1385.

Matsuoka, S., Ballif, B.A., Smogorzewska, A., McDonald, E.R., 3rd, Hurov, K.E., Luo, J., Bakalarski, C.E., Zhao, Z., Solimini, N., Lerenthal, Y., et al. (2007). ATM and ATR substrate analysis reveals extensive protein networks responsive to DNA damage. Science *316*, 1160–1166.

Olma, M.H., Roy, M., Le Bihan, T., Sumara, I., Maerki, S., Larsen, B., Quadroni, M., Peter, M., Tyers, M., and Pintard, L. (2009). An interaction network of the mammalian COP9 signalosome identifies Dda1 as a core subunit of multiple Cul4-based E3 ligases. J. Cell Sci. *122*, 1035–1044.

Pick, E., Hofmann, K., and Glickman, M.H. (2009). PCI complexes: Beyond the proteasome, CSN, and eIF3 Troika. Mol. Cell *35*, 260–264.

Read, M.A., Brownell, J.E., Gladysheva, T.B., Hottelet, M., Parent, L.A., Coggins, M.B., Pierce, J.W., Podust, V.N., Luo, R.S., Chau, V., and Palombella, V.J. (2000). Nedd8 modification of cul-1 activates SCF(beta(TrCP))-dependent ubiquitination of IkappaBalpha. Mol. Cell. Biol. *20*, 2326–2333.

Roy, A., Kucukural, A., and Zhang, Y. (2010). I-TASSER: a unified platform for automated protein structure and function prediction. Nat. Protoc. *5*, 725–738.

Russo, A.A., Jeffrey, P.D., Patten, A.K., Massagué, J., and Pavletich, N.P. (1996). Crystal structure of the p27Kip1 cyclin-dependent-kinase inhibitor bound to the cyclin A-Cdk2 complex. Nature *382*, 325–331.

Saha, A., and Deshaies, R.J. (2008). Multimodal activation of the ubiquitin ligase SCF by Nedd8 conjugation. Mol. Cell *32*, 21–31.

Sato, Y., Yoshikawa, A., Yamagata, A., Mimura, H., Yamashita, M., Ookata, K., Nureki, O., Iwai, K., Komada, M., and Fukai, S. (2008). Structural basis for specific cleavage of Lys 63-linked polyubiquitin chains. Nature *455*, 358–362.

Scheel, H., and Hofmann, K. (2005). Prediction of a common structural scaffold for proteasome lid, COP9-signalosome and eIF3 complexes. BMC Bioinformatics *6*, 71.

Schmidt, M.W., McQuary, P.R., Wee, S., Hofmann, K., and Wolf, D.A. (2009). F-box-directed CRL complex assembly and regulation by the CSN and CAND1. Mol. Cell *35*, 586–597.

Schulman, B.A., Carrano, A.C., Jeffrey, P.D., Bowen, Z., Kinnucan, E.R., Finnin, M.S., Elledge, S.J., Harper, J.W., Pagano, M., and Pavletich, N.P. (2000). Insights into SCF ubiquitin ligases from the structure of the Skp1-Skp2 complex. Nature *408*, 381–386.

Scott, D.C., Monda, J.K., Bennett, E.J., Harper, J.W., and Schulman, B.A. (2011). N-terminal acetylation acts as an avidity enhancer within an interconnected multiprotein complex. Science *334*, 674–678.

Serino, G., Su, H., Peng, Z., Tsuge, T., Wei, N., Gu, H., and Deng, X.W. (2003). Characterization of the last subunit of the Arabidopsis COP9 signalosome: implications for the overall structure and origin of the complex. Plant Cell *15*, 719–731.

Sharon, M., Mao, H., Boeri Erba, E., Stephens, E., Zheng, N., and Robinson, C.V. (2009). Symmetrical modularity of the COP9 signalosome complex suggests its multifunctionality. Structure *17*, 31–40.

Siergiejuk, E., Scott, D.C., Schulman, B.A., Hofmann, K., Kurz, T., and Peter, M. (2009). Cullin neddylation and substrate-adaptors counteract SCF inhibition by the CAND1-like protein Lag2 in Saccharomyces cerevisiae. EMBO J. *28*, 3845–3856.

Spruck, C., Strohmaier, H., Watson, M., Smith, A.P., Ryan, A., Krek, T.W., and Reed, S.I. (2001). A CDK-independent function of mammalian Cks1: targeting of SCF(Skp2) to the CDK inhibitor p27Kip1. Mol. Cell *7*, 639–650.

Sun, Y., Wilson, M.P., and Majerus, P.W. (2002). Inositol 1,3,4-trisphosphate 5/6-kinase associates with the COP9 signalosome by binding to CSN1. J. Biol. Chem. *277*, 45759–45764.

Tenbaum, S.P., Juenemann, S., Schlitt, T., Bernal, J., Renkawitz, R., Muñoz, A., and Baniahmad, A. (2003). Alien/CSN2 gene expression is regulated by thyroid hormone in rat brain. Dev. Biol. *254*, 149–160.

Tron, A.E., Arai, T., Duda, D.M., Kuwabara, H., Olszewski, J.L., Fujiwara, Y., Bahamon, B.N., Signoretti, S., Schulman, B.A., and DeCaprio, J.A. (2012). The glomuvenous malformation protein Glomulin binds Rbx1 and regulates cullin RING ligase-mediated turnover of Fbw7. Mol. Cell *46*, 67–78.

Tsuge, T., Matsui, M., and Wei, N. (2001). The subunit 1 of the COP9 signalosome suppresses gene expression through its N-terminal domain and incorporates into the complex through the PCI domain. J. Mol. Biol. *305*, 1–9.

Uhle, S., Medalia, O., Waldron, R., Dumdey, R., Henklein, P., Bech-Otschir, D., Huang, X., Berse, M., Sperling, J., Schade, R., and Dubiel, W. (2003). Protein kinase CK2 and protein kinase D are associated with the COP9 signalosome. EMBO J. *22*, 1302–1312.

Wilson, M.P., Sun, Y., Cao, L., and Majerus, P.W. (2001). Inositol 1,3,4-trisphosphate 5/6-kinase is a protein kinase that phosphorylates the transcription factors c-Jun and ATF-2. J. Biol. Chem. *276*, 40998–41004.

Yamoah, K., Oashi, T., Sarikas, A., Gazdoiu, S., Osman, R., and Pan, Z.Q. (2008). Autoinhibitory regulation of SCF-mediated ubiquitination by human cullin 1's C-terminal tail. Proc. Natl. Acad. Sci. USA *105*, 12230–12235.

Yang, X., Menon, S., Lykke-Andersen, K., Tsuge, T., Di Xiao, Wang, X., Rodriguez-Suarez, R.J., Zhang, H., and Wei, N. (2002). The COP9 signalosome inhibits p27(kip1) degradation and impedes G1-S phase progression via deneddylation of SCF Cul1. Curr. Biol. *12*, 667–672.

Zheng, N., Wang, P., Jeffrey, P.D., and Pavletich, N.P. (2000). Structure of a c-Cbl-UbcH7 complex: RING domain function in ubiquitin-protein ligases. Cell *102*, 533–539.

Zheng, N., Schulman, B.A., Song, L., Miller, J.J., Jeffrey, P.D., Wang, P., Chu, C., Koepp, D.M., Elledge, S.J., Pagano, M., et al. (2002). Structure of the Cul1-Rbx1-Skp1-F boxSkp2 SCF ubiquitin ligase complex. Nature *416*, 703–709.

Cell PRESS
Open ACCESS

EXTENDED EXPERIMENTAL PROCEDURES

Protein Expression and Purification

CSN expression constructs used in this study were prepared using the MultiBac system, following the strategy described in (Enchev et al., 2010). However, we substituted the C-terminal StrepII-tag on Csn3 for an N-terminal StrepII^{2x}-tag, which significantly increased purification yields. Moreover, only one isoform of Csn7, Csn7b, was included to increase structural homogeneity. Thus, wild-type CSN and the active site mutated CSN^{Csn5H138A} constructs were generated from pUCDM-Csn2/^{StrepII2x}3/6/8 and pFBDM-Csn1/4/^{His6}5$^{wt\ or\ H138A}$/7b. For the CSN constructs harboring Csn5 deletion or N-terminal Csn2 truncations we used only pFBDM transfer vectors with the following cassettes: Csn4/7b; Csn1/^{His6}5$^{wt\ or\ H138A\ or\ missing}$; Csn^{StrepII2x}3/2$^{wt\ or\ N\text{-}terminally\ truncated}$; Csn6/8. DNA sequences for all individual proteins were verified as wild-type or the desired mutants by sequencing. Restriction digests were used to control correct assembly of the MultiBac transfer vectors.

A single baculovirus for each of the CSN variants was produced, amplified, expressed and purified over a Strep-Tactin Superflow Cartridge (QIAGEN) as described in (Enchev et al., 2010). Due to the increased purification yields after the affinity column, the CSN purification protocol was enhanced by the following steps: the StrepII^{2x} tag was usually cleaved at this stage, all fractions were pooled and PreScission protease was added in a 1:50 molar ratio. Cleavage was performed overnight in a dialysis tube in 2 L dialysis buffer (25 mM HEPES, pH 7.5, 150 mM NaCl, 2% glycerol, 2 mM DTT). The pooled Strep-Tactin elution fractions (cleaved or uncleaved) were concentrated to 5 ml with a 50 kDa cut-off concentrator (Amicon) and loaded on a Sephacryl 300 16/60 size-exclusion column (GE Healthcare) buffer exchanging into 15 mM HEPES pH 7.5, 200 mM NaCl, 2% glycerol and 2 mM DTT. Fractions from the first Sephacryl 300 peak were pooled and diluted to 50 ml in buffer A (15 mM HEPES pH 7.5, 50 mM NaCl, 2% glycerol, 2 mM DTT). This protein solution was loaded with a 50 ml superloop onto a 6ml ResourceQ anion-exchange column (GE Healthcare) and eluted using a gradient from 50 to 400 mM NaCl over 40 CV with buffer B (15 mM HEPES pH 7.5, 1 M NaCl, 2% glycerol, 2 mM DTT). If the sample was used for EM analysis, an additional Superose 6 10/300 size-exclusion (GE Healthcare) purification step was performed with the peak fraction from the ResourceQ run. Fractions were usually sufficiently concentrated and no additional concentrating step was required. The fraction was loaded with a 500 μl loop, buffer exchanging back to 15 mM HEPES pH 7.8, 150 mM NaCl, 1% glycerol and 1 mM DTT. Typical CSN yields after this step were between 5 and 10 mg from 1 L of High Five cells. The sample was either aliquoted, flash frozen in liquid nitrogen and stored at −80°C or directly used for EM analysis.

The full-length ^{StrepII2x}Cul1/Rbx1 baculovirus expression construct was generated, expressed and purified as described in (Enchev et al., 2010).

Split-and-coexpress Cul1/Rbx1; split-and-coexpress Cul1$^{\Delta WHB}$/Rbx1; split-and-coexpress Cul1/Rbx1$^{\Delta RING}$; Cul1^{CTD}/Rbx1; Cul1^{WHB}; Cks1; CyclinA; Cdk2; and p27 as well as neddylation and ubiquitination reagents were generated, expressed and purified as described in (Duda et al., 2008). Human Ubc12 was expressed in insect cells and purified on a C-terminal His6-tag. Analogously to its yeast homolog (Scott et al., 2011) Ubc12 was thus purified in an N-terminally acetylated state. Assembly of Skp1/F-box expression constructs was achieved by cloning either full-length Skp2 or Fbw7$^{\Delta N1\text{-}263}$ into pGEX4T1-TEV with EcoRI/SalI. Full-length Skp1 was cloned into the NotI/NotI sites of the respective pGEX4T1-TEV Fbw7$^{\Delta N1\text{-}263}$ or Skp2$^{full\text{-}length}$ vectors. Recombinant baculoviruses were generated by standard procedures and the protein was produced by coinfection of Sf9 insect cells. Skp1/F-box heterodimeric complexes were affinity-purified over gluthatione sepharose beads (GE Healthcare), the GST-tag was cleaved with TEV and Skp1/F-box was further purified over ResourceQ ion exchange and Superdex200 size-exclusion chromatography. A common chaperone contaminant, DnaK, was usually removed by supplementing the running buffer with 2 mM ATP and 10 mM $MgCl_2$ before using Skp1/F-box constructs for CSN interaction studies or structural analysis.

Variant CSN-SCF complexes for EM data collection were purified over two steps. First the CSN variant purified over the affinity, ion exchange and size-exclusion chromatography steps but with an un-cleaved StrepII^{2x} tag on Csn3 was immobilized on a 1 ml Strep-Tactin Superflow Cartridge with the Superose 6 buffer described above. After washing with 10 CV, the SCF variant with cleaved StrepII^{2x} tag on Cul1 was loaded in two- to three-fold molar excess. Following a wash with 10 CV, the complexes were eluted by supplementing the buffer with 2.5 mM desthiobiotin in 200 μl fractions. Without further concentration the two peak fractions were loaded onto a Superose 6 10/300 size-exclusion column and the peak fraction sample was used for electron microscopy.

Antibodies

Antibodies against CSN subunits were purchased as a sampler pack (Enzo LifeSciences, BML-PW8945-0001). Antibodies against Cullin1 were either from Rockland Immunochemicals (C-terminal specific, cat #100-401-A01) or from Santa Cruz Biotechnology (AS97, cat # sc-12761 and H-213, cat # sc-11384); anti-Skp1 from Santa Cruz Biotechnology (N-19, cat # sc-1569); anti-Skp2 from Zymed (cat #51-1900), anti-Fbw7 from AbNova (cat # H00055294-MO2); anti-p27 from Santa Cruz Biotechnology (N-20, cat # sc-527); anti phospho-p27 from Santa Cruz Biotechnology (Thr187, cat # sc-16324); anti-CyclinA from Santa Cruz Biotechnology (H-432, cat # sc-751); anti-Cdk2 from Santa Cruz Biotechnology (G-298, cat # sc-748); anti-CAND1 from Rockland Immunochemicals (N-terminal specific, cat #100-401-A11); anti-ubiquitin from Santa Cruz Biotechnology (P4D1) and anti-His_5 from QIAGEN (cat #34698). The anti-Nedd8 antibody was as described in (Souphron et al., 2008).

Secondary antibodies (anti-mouse, anti-rabbit and anti-goat) were HP-conjugated and purchased from GE Healthcare (respectively cat# NA9310, NA934 and PA42002).

Immunoblotting and Quantifications

Immunoblots developed with ECL Plus (GE Healthcare) were scanned on a Phosphoimager, whereas immunoblots developed on film were subsequently scanned and quantified using ImageJ (rsbweb.nih.gov/ij/). The signal intensity for the de-neddylated Cul1 band formed at the last time point was set to be 100%, and the signals for all other bands in the gel normalized to that value.

Deubiquitination Assays

In the de-ubiquitination assay (Figure S6E) we used 30 ng/μl of the K48-linked poly-ubiquitin chains (BostonBiochem, uc-220), which corresponds approximately to 1 μM, and 500 nM $CSN^{Csn5H138A}$ or recombinantly produced and purified catalytic domain of Usp2 (a kind gift by S. Kaiser and R. Kopito).

Negative Stain Electron Microscopy

Quantifoil grids (R2/2 Cu 400 mesh) coated with thin carbon floated from mica were glow-discharged for 30 s at 50 mA and 0.2 mbar vacuum. 3 μl purified samples were applied for 1 min to the grids. Following two brief buffer washes, the grids were stained with 2% uranyl acetate, gently blotted using filter paper and air-dried.

Images were collected with a Tecnai F20 electron microscope (FEI) on a 4k x 4k CCD detector (Tietz) at a nominal magnification of 50,000 and an underfocus level that placed the first minimum in the contrast transfer function at 18 Å. Images were binned by a factor of two, resulting in a pixel size of 3.47 Å at the specimen level. Low dose settings were used exposing with ~100 $e^{-}/Å^2$ which significantly improved the signal-to-noise ratio without incurring a loss of structural information to the resolution of the current study.

Single-Particle Analysis

Single molecular views were chosen manually from the micrographs using Boxer, part of EMAN (Ludtke et al., 1999). A total of 8055 images were collected for the CSN-SCF~$N8^{Skp2/Cks1}$ data set; 4761 for the CSN-SCF~$N8^{Fbw7}$ data set; 5165 for the $CSN^{Csn5H138A}$ data set; 4379 for the $CSN^{Csn2\Delta N1\text{-}269}$ data set and 3106 for the $CSN^{\Delta Csn5}$-SCF~$N8^{Skp2/Cks1}$ data set. The data stacks were high-pass filtered at 1/250 $Å^{-1}$, masked with a circle and normalized to zero mean and standard deviation of 2 in IMAGIC-5 (van Heel et al., 1996) and low-pass filtered at 1/15 $Å^{-1}$ with the fq command SPIDER (Frank et al., 1996), choosing the Fermi filter option.

Initial classification was performed with the reference-free classification routine refine2d from EMAN. Different sets of three different class averages with high signal-to-noise ratio were selected and submitted to the C1 start up routine in IMAGIC until the program returned near orthogonal Euler angle assignments. A 3D reconstruction from those three class averages was calculated in IMAGIC and the three corresponding re-projections were used as an anchor set for assigning Euler angles to the remaining initial class averages. The calculated 3D model was used as the starting point for refinement.

Refinement consisted of iterated rounds of multi-reference alignment performed in SPIDER, multivariate statistical analysis (MSA) of the newly aligned data set followed by hierarchical ascendant classification and angular assignment through projection-matching performed in IMAGIC. The agreement between the appearance of class averages and corresponding structure re-projections was used as a manual selection criterion before calculating the final 3D reconstruction of each refinement round.

Three-Dimensional Reconstructions

Three-Dimensional Reconstructions were calculated using a locally developed program, described in detail below.

In single particle analysis, three-dimensional reconstruction from a set of projection images is typically carried out by weighted back projection. In this process the individual two-dimensional projection images are back projected into the reconstructed three-dimensional volume in directions defined by Euler angles, which have been assigned as part of the analysis. The reconstruction is obtained by summing all of these contributions. A weighting procedure is required to correct for the resulting inherent unequal distribution of contributed data at different spatial frequencies. The exact filter three-dimensional reconstruction procedure of (Harauz and van Heel, 1986) takes account of this effect as well as allowing for any unequal angular distribution of the input data. This is achieved by considering the equivalence between two-dimensional projections of a three-dimensional object in real space and central sections of its three-dimensional Fourier transform (the central section theorem). For a finite object, each such Fourier central section has a depth, which is reciprocally related to the dimension of the reconstructed object in the direction of projection. From these considerations two-dimensional weighting functions in Fourier space can be evaluated which take account of the overlapping contributions from the rest of the data set for each Fourier coefficient of an input image. These weighting (or filter) functions are then used to filter the Fourier transforms of each of the input images which are then transformed back into real space and back projected.

The Fourier space three-dimensional reconstruction used here represents an implementation of the weighting scheme described by (Harauz and van Heel, 1986) but in this case the weighting is applied directly to the three-dimensional Fourier transform of the reconstructed volume. Fourier transforms of each input image undergo a coordinate transformation defined by their assigned Euler angles thereby creating central sections through the three-dimensional transform. Contributions from each coefficient of the Fourier transform of the input images are added to the three-dimensional Fourier transform using a geometrical weighting function (w_g) derived from the fractional distance between the input Fourier coefficient and the output three-dimensional Fourier coefficient (df)

expressed as a fraction of the reciprocal extent of the reconstructed object (do) measured in the direction of the vector between the Fourier coefficients.

$$w_g = \mathrm{sinc}\left(\pi \cdot \left(\frac{df}{do}\right)\right)$$

The three-dimensional Fourier transform of the reconstructed volume is evaluated by summing the weighted contributions of all the input data in a manner similar to the procedure used by FREEALIGN program (Grigorieff, 2007)

$$F_{3D} = \frac{\left(\sum F_{2D}.w_g\right)}{\left(f + \sum w_g\right)}.$$

Where F_{3D} is a Fourier coefficient of the three-dimensional Fourier transform of the reconstructed volume, F_{2D} are the Fourier coefficients of the input images and f is a constant (similar to a Weiner filter), typically set to 0.1 of the mean value of w_g, which is included to avoid overrepresentation of sparse data. Additional weighting terms are included to take account of the contrast transfer function (CTF) and to allow effective CTF amplitude correction of data from unstained cryo-electron microscope images. However, these are not relevant to the analysis of negative stained data and are not described here. To increase the accuracy of the procedure the Fourier transforms of both the input images and the three-dimensional reconstruction are subsampled by padding the input images in boxes n x the original dimensions. A typical value for n is 2. Once all the input data have been merged in Fourier space the three-dimensional reconstruction in real space is obtained by Fourier transformation. The program, icrmake3d, is written in C++, reads input images and their Euler angles in Imagic format and outputs a three-dimensional reconstruction in Imagic format.

The resulting three-dimensional reconstructions are characterized by a cleaner background while retaining at least as good a recovery of detail compared to other readily accessible software.

Difference Map Analysis

Difference map analysis was performed in IMAGIC. The respective binary masked maps were aligned to each other in three dimensions, normalized to the same standard deviation and subtracted. The resultant difference density was low-pass filtered at 1/25 $Å^{-1}$ and displayed in Chimera at similar contour levels to the corresponding reconstructions. The segmentations shown in Figure S1D were determined via overlays with the corresponding CSN-SCF maps.

Structure Visualization and Docking of Atomic Coordinates into EM Map

UCSF Chimera (Goddard et al., 2007) and Pymol (www.pymol.org) were used for visualization of EM maps and figure generation. Atomic coordinates of X-ray crystallographic structures and/or EM maps were docked into the electron density of the EM maps in UCSF Chimera using the fit in map function. Agreement between maps and fitted coordinates was quantitatively evaluated within local masks using Uro (Navaza et al., 2002).

SUPPLEMENTAL REFERENCES

da Fonseca, P.C., He, J., and Morris, E.P. (2012). Molecular model of the human 26S proteasome. Mol. Cell *46*, 54–66.

Duda, D.M., Borg, L.A., Scott, D.C., Hunt, H.W., Hammel, M., and Schulman, B.A. (2008). Structural insights into NEDD8 activation of cullin-RING ligases: conformational control of conjugation. Cell *134*, 995–1006.

Duda, D.M., Olszewski, J.L., Tron, A.E., Hammel, M., Lambert, L.J., Waddell, M.B., Mittag, T., Decaprio, J.A., and Schulman, B.A. (2012). Structure of a Glomulin-RBX1-CUL1 complex: inhibition of a RING E3 ligase through masking of its E2-binding surface. Mol. Cell *47*, 371–382.

Enchev, R.I., Schreiber, A., Beuron, F., and Morris, E.P. (2010). Structural insights into the COP9 signalosome and its common architecture with the 26S proteasome lid and eIF3. Structure *18*, 518–527.

Frank, J., Radermacher, M., Penczek, P., Zhu, J., Li, Y., Ladjadj, M., and Leith, A. (1996). SPIDER and WEB: processing and visualization of images in 3D electron microscopy and related fields. J. Struct. Biol. *116*, 190–199.

Goddard, T.D., Huang, C.C., and Ferrin, T.E. (2007). Visualizing density maps with UCSF Chimera. J. Struct. Biol. *157*, 281–287.

Grigorieff, N. (2007). FREALIGN: high-resolution refinement of single particle structures. J. Struct. Biol. *157*, 117–125.

Gusmaroli, G., Figueroa, P., Serino, G., and Deng, X.W. (2007). Role of the MPN subunits in COP9 signalosome assembly and activity, and their regulatory interaction with *Arabidopsis* Cullin3-based E3 ligases. Plant Cell *19*, 564–581.

Harauz, G., and van Heel, M. (1986). Exact filters for general geometry three dimensional reconstruction. Optik *73*, 146–156.

Ludtke, S.J., Baldwin, P.R., and Chiu, W. (1999). EMAN: semiautomated software for high-resolution single-particle reconstructions. J. Struct. Biol. *128*, 82–97.

Navaza, J., Lepault, J., Rey, F.A., Alvarez-Rúa, C., and Borge, J. (2002). On the fitting of model electron densities into EM reconstructions: a reciprocal-space formulation. Acta Crystallogr. D Biol. Crystallogr. *58*, 1820–1825.

Pathare, G.R., Nagy, I., Bohn, S., Unverdorben, P., Hubert, A., Körner, R., Nickell, S., Lasker, K., Sali, A., Tamura, T., et al. (2012). The proteasomal subunit Rpn6 is a molecular clamp holding the core and regulatory subcomplexes together. Proc. Natl. Acad. Sci. USA *109*, 149–154.

Roy, A., Kucukural, A., and Zhang, Y. (2010). I-TASSER: a unified platform for automated protein structure and function prediction. Nat. Protoc. *5*, 725–738.

Scott, D.C., Monda, J.K., Bennett, E.J., Harper, J.W., and Schulman, B.A. (2011). N-terminal acetylation acts as an avidity enhancer within an interconnected multiprotein complex. Science *334*, 674–678.

Souphron, J., Waddell, M.B., Paydar, A., Tokgöz-Gromley, Z., Roussel, M.F., and Schulman, B.A. (2008). Structural dissection of a gating mechanism preventing misactivation of ubiquitin by NEDD8's E1. Biochemistry *47*, 8961–8969.

van Heel, M., Harauz, G., Orlova, E.V., Schmidt, R., and Schatz, M. (1996). A new generation of the IMAGIC image processing system. J. Struct. Biol. *116*, 17–24.

Zheng, N., Schulman, B.A., Song, L., Miller, J.J., Jeffrey, P.D., Wang, P., Chu, C., Koepp, D.M., Elledge, S.J., Pagano, M., et al. (2002). Structure of the Cul1-Rbx1-Skp1-F boxSkp2 SCF ubiquitin ligase complex. Nature *416*, 703–709.

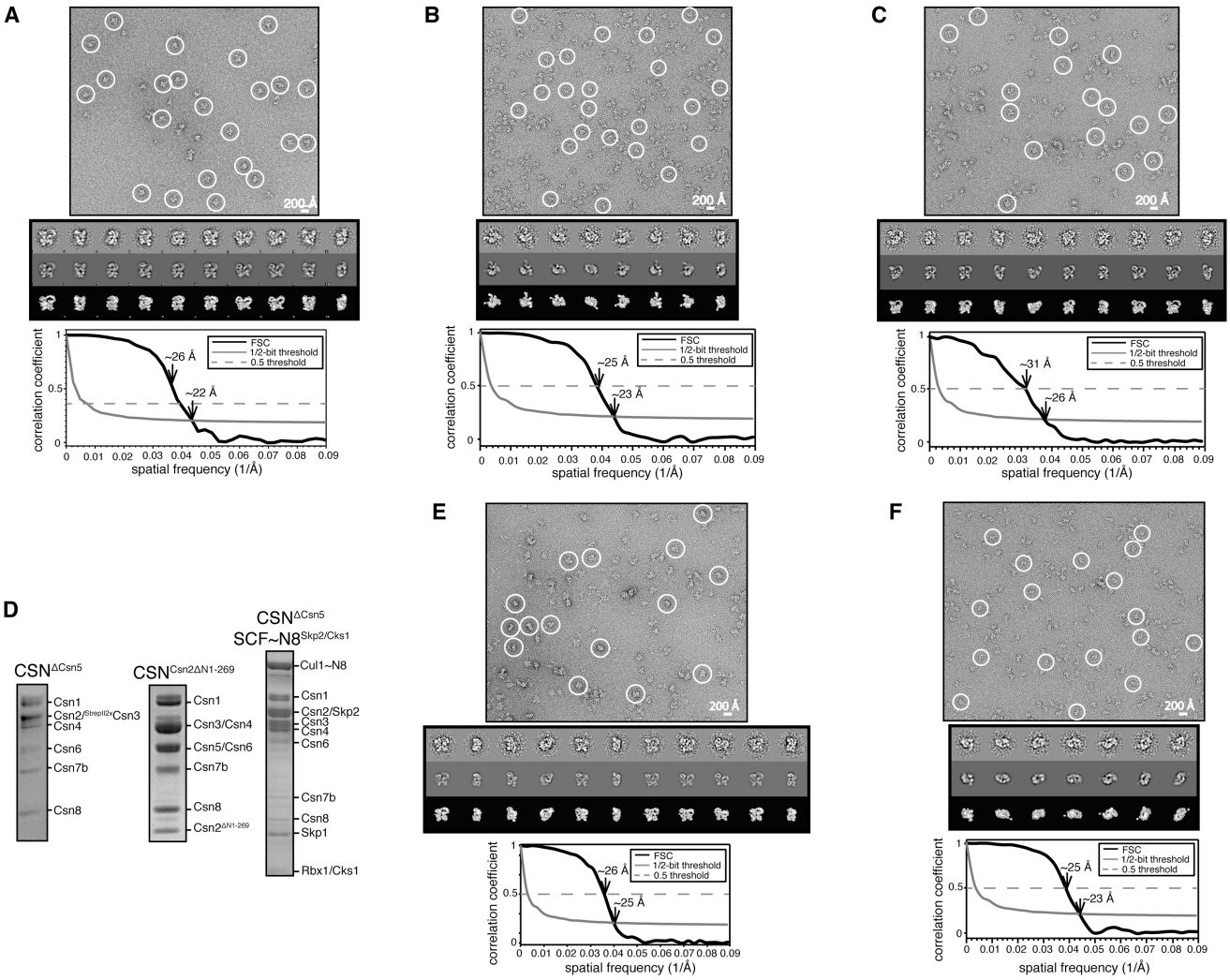

Figure S1. Single Particle Electron Microscopy Analysis of CSN-SCF Complexes, Related to Figure 1

(A–C, E, and F) Electron microscopy and single particle analysis of the (A) CSN^{Csn5H138A}-SCF∼N8$^{Skp2/Cks1}$, (B) CSN^{Csn5H138A}, (C) CSN^{Csn5H138A}-SCF∼N8^{Fbw7}, (E) CSN$^{\Delta Csn5}$-SCF∼N8$^{Skp2/Cks1}$, and (F) CSN$^{Csn2\Delta N1\text{-}269}$ data sets. Characteristic electron micrographs in negative stain are shown in the top panel. Circles indicate examples of molecular images. The middle panels show a representative selection of refined class averages (top), re-projections of the 3D structure (middle) and corresponding surface views (bottom row). Fourier Shell Correlation based resolution estimates are shown in the bottom panels.

(D) Coomassie-stained SDS-PAGE of the recombinant CSN$^{\Delta Csn5}$ and CSN$^{Csn2\Delta N1\text{-}269}$ as well as the in vitro reconstituted CSN$^{\Delta Csn5}$-SCF∼N8$^{Skp2/Cks1}$ complex after size-exclusion chromatography.

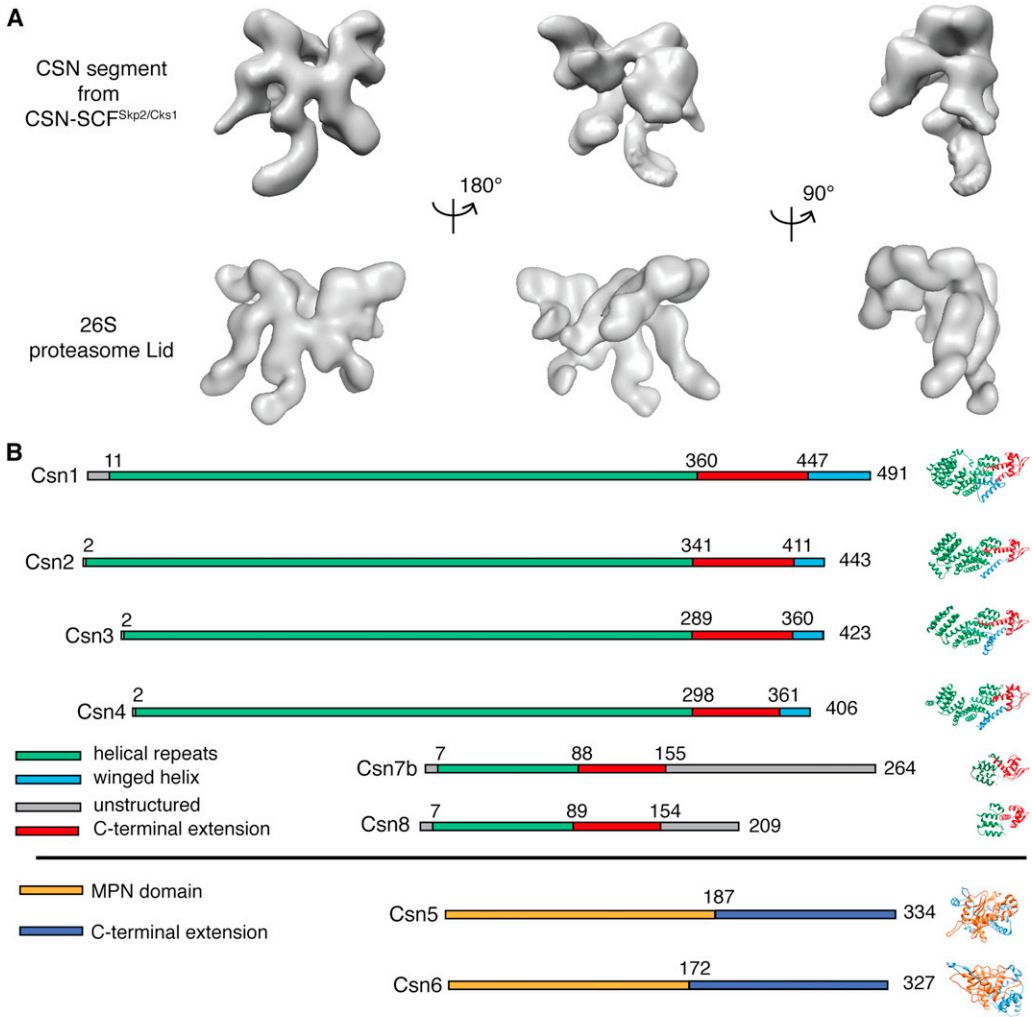

subunit	correlation coefficient
Csn1	0.76
Csn2	0.85
Csn3	0.82
Csn4	0.79
Csn5	0.93
Csn6	0.87
Csn7	0.98
Csn8	0.98
Cul1	0.93
Skp1	0.98
Skp2	0.98
Cks1	0.99

Figure S2. Supporting Data for the CSN Molecular Model, Related to Figure 2

(A) Orthogonal surface views of the CSN segment from the CSN^{Csn5H138A}-SCF∼N8$^{Skp2/Cks1}$ map (top) and the 26S proteasome Lid (bottom) from (da Fonseca et al., 2012), shown in similar orientations.

(B) Atomic models for CSN subunits generated by the I-Tasser structural prediction server (Roy et al., 2010) and corresponding diagrams of the domain distribution.

(C) Atomic models for the N-terminally truncated Csn2 constructs. The N-terminus of Csn2 was predicted to comprise a capping N-terminal α-helix, followed by six helical-repeat motifs. Note the similarity to the N-terminus of the recently solved structure of the Csn2 paralogue Rpn6, which also contains a capping N-terminal helix, followed by five TPR-like helical repeats (Pathare et al., 2012). The three truncation constructs used in this study are thus predicted to be lacking the capping helix and two (CSN$^{Csn2ΔN1-104}$), four (CSN$^{Csn2ΔN1-185}$) or six (CSN$^{Csn2ΔN1-269}$) TPR- like motifs.

(D) Quantitative evaluation of the fit of the atomic models for the indicated subunits in the CSN^{Csn5H138A}-SCF∼N8$^{Skp2/Cks1}$ map. Correlation coefficients were calculated within local masks over the resolution range 400 – 25 Å using the program Uro (Navaza et al., 2002). The correlation coefficients for the smallest subunits, Csn7 and Csn8, as well as Skp1 and Cks1 are anomalously high due to their globular shape and the limited resolution of the current analysis.

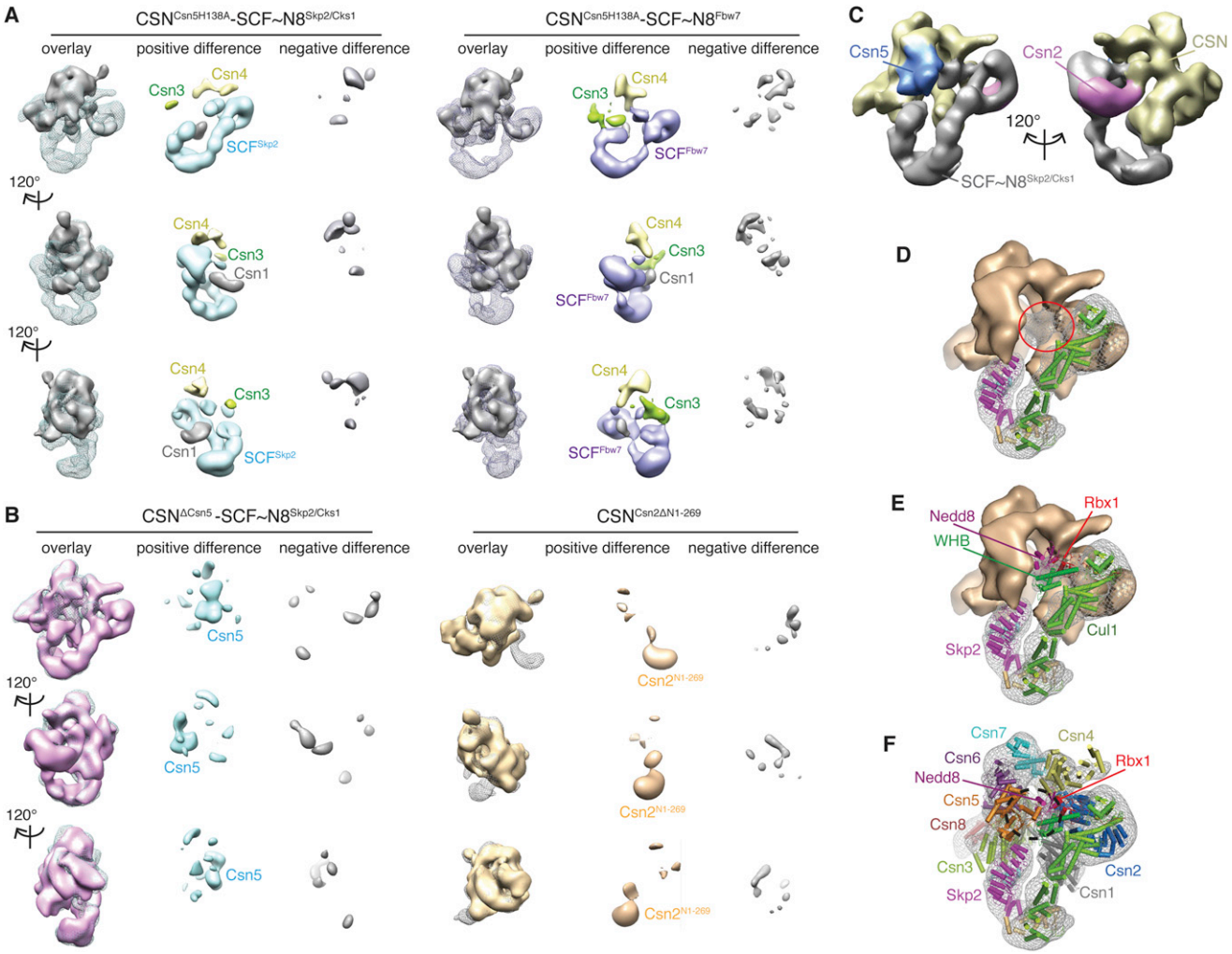

Figure S3. Difference Map Analysis and Nedd8 Docking, Related to Figures 1 and 3

(A) Structural comparison (left) and difference map analysis (middle and right) between (left hand side) $CSN^{Csn5H138A}$-SCF∼$N8^{Skp2/Cks1}$ (cyan mesh) and $CSN^{Csn5H138A}$ (gray surface) to locate the CSN segment in the $CSN^{Csn5H138A}$-SCF∼$N8^{Skp2/Cks1}$ map; and (right hand side) of $CSN^{Csn5H138A}$-SCF∼$N8^{Fbw7}$ (purple mesh) and $CSN^{Csn5H138A}$ (gray surface) to locate the CSN segment in the $CSN^{Csn5H138A}$-SCF∼$N8^{Fbw7}$ map. Within the difference maps the segments corresponding to the SCF∼$N8S^{kp2/Cks1}$ and SCF∼$N8^{Fbw7}$ are color-coded in cyan and purple; difference densities within the regions interpreted as Csn1, Csn3 and Csn4 (see Figure 2) are shown in gray, green and yellow respectively. Interestingly, Csn1 and Csn3 and perhaps also Csn4 are involved in SCF binding (see Discussion and (Gusmaroli et al., 2007)).

(B) Structural comparison (left) and difference map analysis (middle and right) between (left hand side) $CSN^{Csn5H138A}$-SCF∼$N8^{Skp2/Cks1}$ (cyan mesh) and $CSN^{\Delta Csn5}$-SCF∼$N8^{Skp2/Cks1}$ (pink surface) to locate Csn5 (cyan surface); and (right hand side) $CSN^{Csn5H138A}$ (gray mesh), and $CSN^{Csn2\Delta N1-269}$ (yellow surface) to locate the Csn^{N1-269} segment (orange surface).

(C) Segmented surface views of the $CSN^{Csn5H138A}$-SCF∼$N8^{Skp2/Cks1}$ map showing the SCF∼$N8^{Skp2/Cks1}$ density segment in gray, the CSN in yellow and the Csn2 and Csn5 regions in pink and blue respectively.

(D–F) Tentative docking of Rbx1, $Cul1^{691-776}$ and Nedd8 into the SCF∼$N8^{Skp2/Cks1}$ segment of the $CSN^{Csn5H138A}$-SCF∼$N8^{Skp2/Cks1}$ map. (D) The density attributed to CSN is shown as an orange surface, the $SCF^{Skp2/Cks1}$∼N8 density is rendered as a gray mesh and the atomic coordinates of individual subunits are color-coded as in (E). After docking the atomic coordinates for $Cul1^{1-690}$-Skp1-Skp2-Cks1, a segment attributed to $SCF^{Skp2/Cks1}$∼N8 located between Csn5, Csn4 and Csn2 is still left empty (red circle). (E) Rbx1 and $Cul1^{691-776}$-Nedd8 (WHB∼N8) can be docked into this segment. The Rbx1 conformation chosen here is as in the non-neddylated Cul1/Rbx1/Skp1/Skp2 model (Zheng et al., 2002) but see also Figure 6A. The position of WHB-N8 was adjusted by rotating helix29, which is known to allow a flexible orientation of the WHB subdomain in neddylated cullins (Duda et al., 2008). (F) The whole $CSN^{Csn5H138A}$-SCF∼$N8^{Skp2/Cks1}$ map is shown as a gray mesh with docked atomic models for all CSN subunits. A dashed circle shows the region where Nedd8 is positioned closely to the active site of Csn5. In this orientation Rbx1 is positioned close to Csn2 and Csn4.

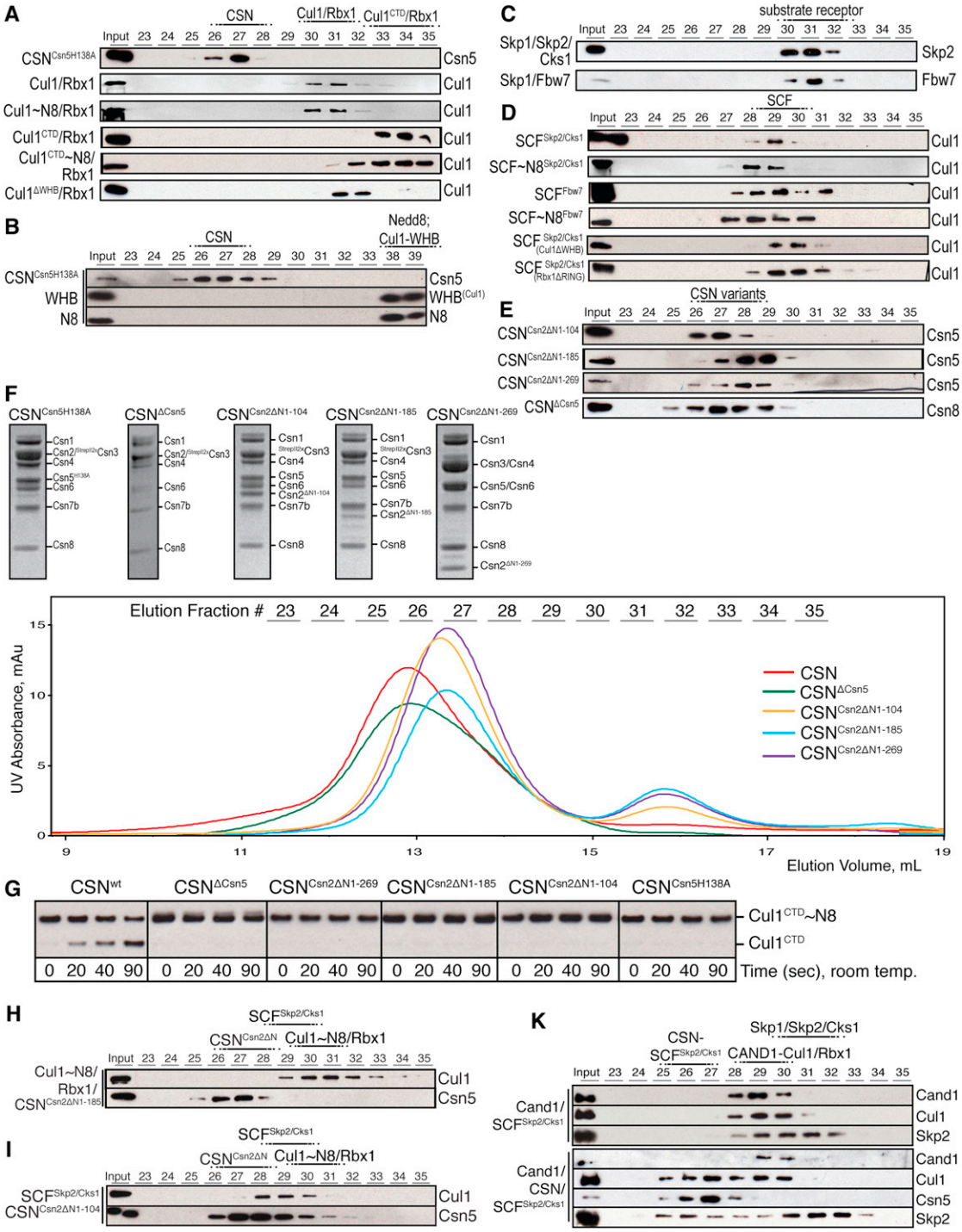

Figure S4. Biochemical Characterization of CSN and SCF Complexes, Related to Figure 4

(A–E) Individual complexes (identified on the left of each blot – neddylated complexes are marked ~N8) were analyzed by analytical size-exclusion chromatography as described for Figure 4. The fractions in which particular complexes were eluted are identified above each blot.

(F) Coomassie-stained SDS-PAGE of the CSN complexes used in this study and overlay of the corresponding Superose6 size-exclusion chromatography profiles. Note that the display of the chromatography profiles (elution volume) is off-set by one fraction.

(G) Deneddylation assays of $Cul1^{CTD}$~N8/Rbx1 with each of the CSN constructs used in this study; neddylated (~N8, upper band) and non-neddylated (lower band) $Cul1^{CTD}$ was visualized by imunnoblotting with anti-Cul1 antibodies.

(H–K) Immunoblot analysis of Superose6 elutions of $CSN^{Csn2\Delta N1-185}$ with Cul1~N8/Rbx1, (H), and $CSN^{Csn2\Delta N1-104}$ with $SCF^{Skp2/Cks1}$, (I), and CAND1-$SCF^{Skp2/Cks1}$ and CSN-CAND1-$SCF^{Skp2/Cks1}$ complexes (K). The labeling scheme is as described in (A–E).

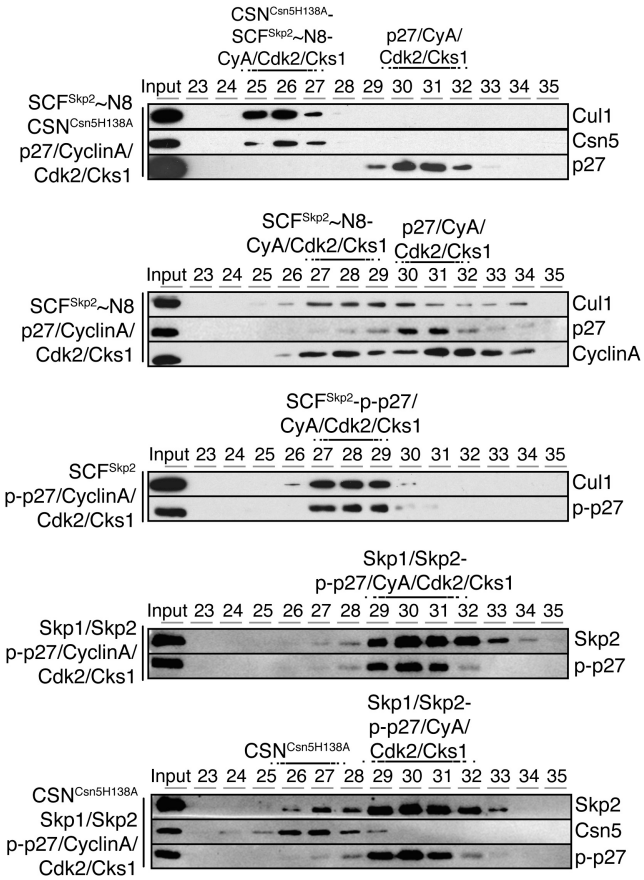

Figure S5. Control Analytical Size-Exclusion Data for the Experiments Presented in Figure 5B, Related to Figure 5

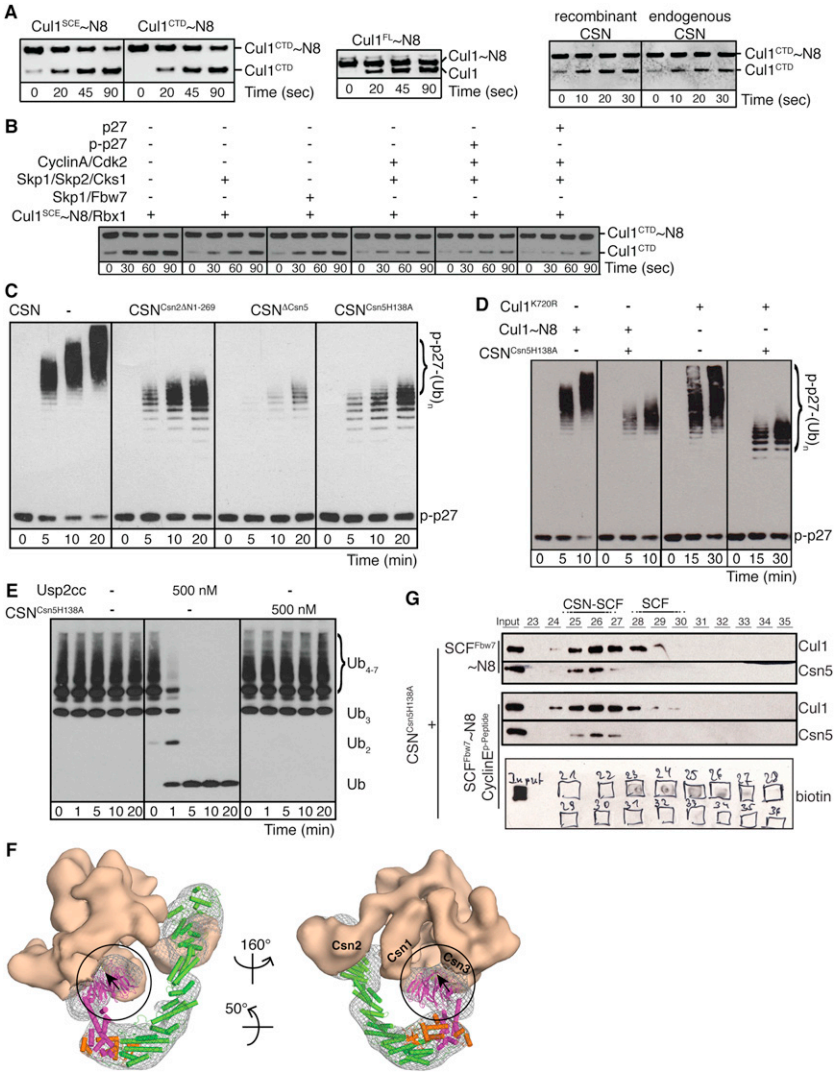

Figure S6. Reciprocal Regulation of CSN and SCF, Related to Figure 6

(A) The deneddylation of full-length (Cul1^{FL}), split-and-coexpressed Cul1 (Cul1^{SCE}) and the Cul1 C-terminal domain (Cul1^{CTD}) by recombinant CSN was analyzed by immunoblotting with Cul1 antibodies (left panels). Note that in contrast to Cul1^{FL}, the two fragments of the Cul1^{SCE} separate upon SDS PAGE analysis, and only the Cul1^{CTD} fragment was probed by immunoblotting. The deneddylation activity of recombinant and endogenous human CSN (purchased from Enzo Life Sciences) were compared, using neddylated Cul1^{CTD} as a substrate (right panel).

(B) The deneddylation of different Cul1^{SCE}~N8/Rbx1 complexes by CSN was monitored by the loss of the Cul1^{CTD}~N8 and the appearance of Cul1^{CTD} using immunoblotting, and quantified by plotting normalized Cul1^{CTD} formation as a function of time.

(C) Poly-ubiquitination of phospho-p27 by SCF~N8$^{Skp2/Cks1}$ in the presence of CSN^{Csn5H138A}, CSN$^{\Delta Csn5}$ or CSN$^{Csn2\Delta N1-269}$. The ubiquitination experiment was performed as described in Figure 6B.

(D) Poly-ubiquitination of phospho-p27 by SCF$^{Skp2/Cks1}$ complexes assembled with either with neddylated wild-type Cul1 (Cul1~N8) or the non-neddylatable Cul1-K720R mutant (Cul1^{K720R}) was measured in the presence (+) or absence (–) of CSN^{Csn5H138A}. Note that CSN^{Csn5H138A} is able to inhibit ubiquitination activity irrespective of the Cul1 neddylation state.

(E) K48-linked poly-ubiquitin chains, containing a mix of three to seven ubiquitin moieties (BostonBiochem), were incubated in buffer or with indicated concentrations of CSN^{Csn5H138A} or the catalytic domain of the K48-specific de-ubiquitinating enzyme Usp2 (Usp2cc). The reaction conditions replicate the experiment in Figures 6B and S6C. De-conjugation of the poly-ubiquitin chains was monitored as a function of time by immunoblotting with anti-ubiquitin antibodies.

(F) Two surface views of the CSN^{Csn5H138A}-SCF~N8^{Fbw7} map at indicated orientations. Modeling of the location of a CyclinE$^{phospho-peptide}$ in the CSN^{Csn5H138A}-SCF~N8^{Fbw7} complex. CSN is shown as an orange surface, the SCF^{Fbw7}~N8 density is rendered as a gray mesh and the atomic coordinates of individual subunits are color-coded as in Figure 3B. The WD40 repeat of Fbw7 is indicated by a circle and the potential position of the CyclinE$^{phospho-peptide}$ is marked by an arrow.

(G) Neddylated (~N8) SCF^{Fbw7} complexes were incubated with equimolar amounts of deneddylation-defective CSN^{Csn5H138A} in the presence (upper panel) or absence (lower panel) of biotinylated CyclinE$^{phospho-peptide}$ as indicated. The complexes were analyzed by size-exclusion chromatography and coelution of Cul1 and Csn5 was followed by immunoblot analysis as described in Figure 4. Coelution of the CyclinE$^{phospho-peptide}$ was analyzed by dot-blot analysis.

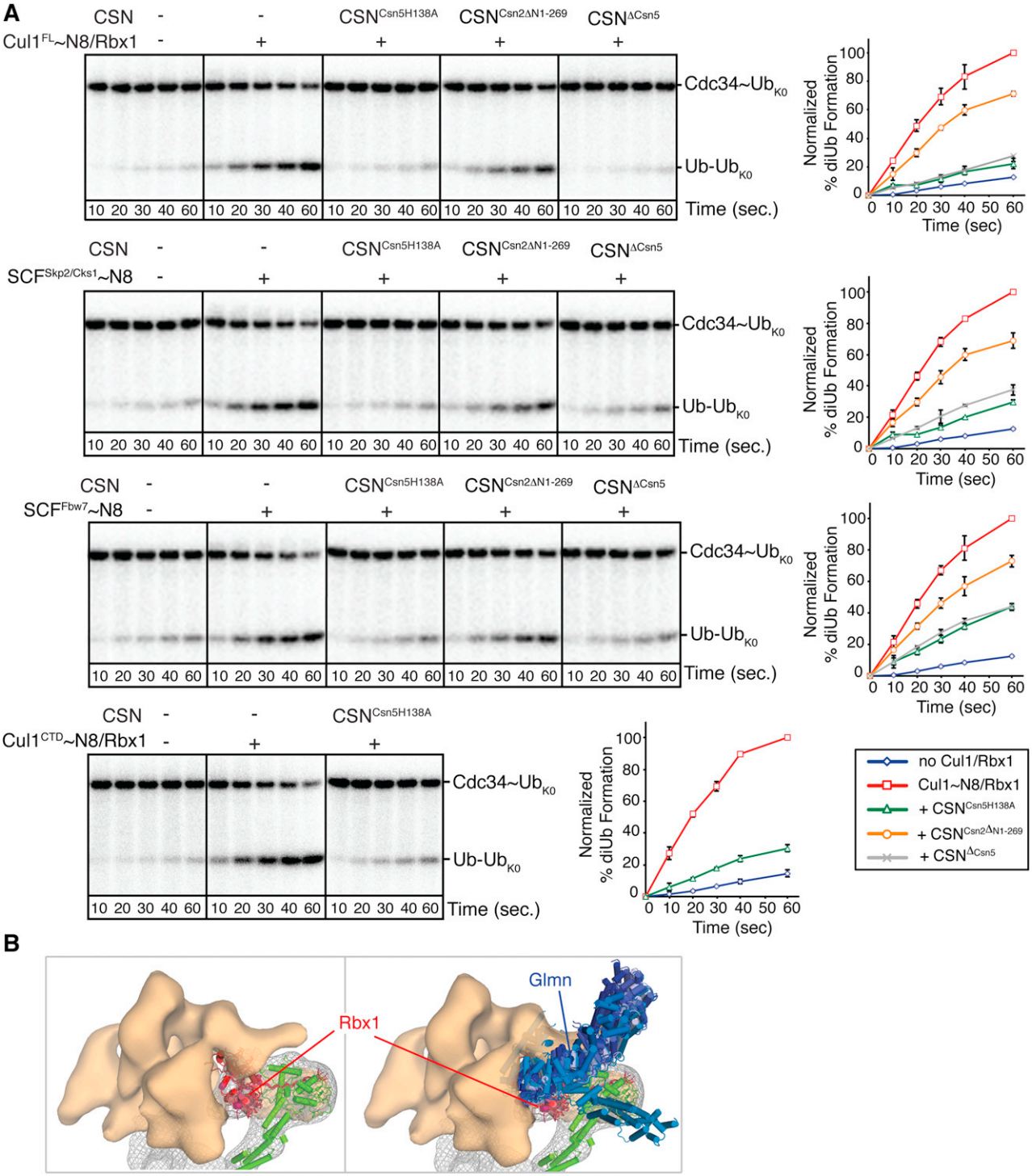

Figure S7. Full Pulse-Chase [^{32}P]~Ubiquitin Transfer Data and Modeling of Glmn Binding to a CSN-SCF Complex, Related to Figure 6

(A) Pulse-chase [^{32}P]~ubiquitin transfer experiment was performed as described in Figure 3B. The ability of neddylated Cul1-species indicated on the left to stimulate Cdc34's intrinsic ubiquitin transfer ability to lysine-less ubiquitin (Ub_{K0}) was assayed in the presence (+) or absence (–) of cullin and the indicated CSN constructs.

(B) A zoomed-in surface view of the CSN^{Csn5H138A}-SCF~N8$^{Skp2/Cks1}$ map, color-coded as in Figure 6A, showing an overlay of all reported Rbx1 conformations without (left) or with docked Glmn model (right). Cul1 (without Helix29 and WHB) is shown in green, Rbx1 orientations are shown as hues of red, Glmn orientations as hues of blue. The Rbx1-Glmn interaction is based on (Duda et al., 2012; PDB identifier 4F52). Note that the Glmn coordinates clash with the electron density assigned to CSN (transparent orange surface) in all orientations, indicating potential steric incompatibility with Glmn binding.